

Extreme flux states of NGC 4151 observed with *INTEGRAL*[★]

P. Lubinski,^{1,2†} A. A. Zdziarski,^{3†} R. Walter,^{2,4} S. Paltani,^{2,4} V. Beckmann,⁵ S. Soldi,⁶
C. Ferrigno² and T. J.-L. Courvoisier^{2,4}

¹Centrum Astronomiczne im. M. Kopernika, Rabiańska 8, PL-87-100 Toruń, Poland

²ISDC Data Centre for Astrophysics, Chemin d'Ecogia 16, CH-1290 Versoix, Switzerland

³Centrum Astronomiczne im. M. Kopernika, Bartycka 18, PL-00-716 Warszawa, Poland

⁴Observatoire de Genève, Université de Genève, Chemin des Maillettes 51, CH-1290 Sauverny, Switzerland

⁵APC, UMR 7164, Université Paris 7 Denis Diderot, 10 rue Alice Domon et Léonie Duquet, F-75025 Paris Cedex 13, France

⁶Laboratoire AIM – CNRS – CEA/DSM – Université Paris Diderot (UMR 7158), CEA Saclay, DSM/IRFU/SAP, F-91191 Gif-sur-Yvette, France

Accepted 2010 June 25. Received 2010 June 25; in original form 2010 May 4

ABSTRACT

We present a comprehensive spectral analysis of all *INTEGRAL* data obtained so far for the X-ray-bright Seyfert galaxy NGC 4151. We also use all contemporaneous data from *RXTE*, *XMM–Newton*, *Swift* and *Suzaku*. We find a linear correlation between the medium- and hard-energy X-ray fluxes measured by *INTEGRAL*, which indicates an almost constant spectral index over 6 yr. The majority of *INTEGRAL* observations were made when the source was either at a very bright or very dim hard–X-ray state. We find that thermal Comptonization models applied to the bright state yields the plasma temperature of $\simeq 50\text{--}70$ keV and its optical depth of $\simeq 1.3\text{--}2.6$, depending on the assumed source geometry. For the dim state, these parameters are in the ranges of $\simeq 180\text{--}230$ keV and $\simeq 0.3\text{--}0.7$, respectively. The Compton parameter is $y \simeq 1$ for all the spectra, indicating a stable geometry. Using this result, we can determine the reflection effective solid angles associated with the close and distant reprocessing media as $\simeq 0.3 \times 2\pi$ and $0.2 \times 2\pi$, respectively. The plasma energy balance, the weak disc reflection and a comparison of the UV fluxes illuminating the plasma to the observed ones are all consistent with an inner hot accretion surrounded by an outer cold disc. The disc truncation radius can be determined from an approximate equipartition between the observed UV and X-ray emission, and from the fitted disc blackbody model, as ~ 15 gravitational radii. Alternatively, our results can be explained by a mildly relativistic coronal outflow.

Key words: accretion, accretion discs – galaxies: active – galaxies: individual: NGC 4151 – galaxies: Seyfert – gamma-rays: general – X-rays: galaxies.

1 INTRODUCTION

Continuum properties of the hard X-ray and soft γ -ray emission from radio-quiet Seyfert galaxies nuclei are relatively well known, thanks to the many satellites operating during the last decades. The spectra are commonly approximated by a phenomenological e-folded power-law model, $F(E) \propto E^{1-\Gamma} \exp(-E/E_c)$ (where Γ is the photon index and E_c is the e-folding, or cut-off, energy), accompanied by a Compton reflection component. A recent study based on a local ($z < 0.1$) sample of 105 Seyfert galaxies observed

with *BeppoSAX* presents the average parameters of this model for Seyfert 1s and 2s (Dadina 2008). The mean Γ is ≈ 1.9 (1.8) for Seyfert 1 (2) nuclei, E_c is $\simeq 230$ (380) keV and the average relative strength of reflection, $R \equiv \Omega/2\pi$ (where Ω is the effective solid angle subtended by the reflector), is $\simeq 1.2$ (0.9). See Beckmann et al. (2009) for the similar *INTEGRAL* results.

This phenomenological model is too crude for studying of the physics of the central engine of Seyferts. There is a general consensus that their $X\gamma$ photons are from (predominantly thermal) Comptonization by hot electrons of some seed soft photons. The seed photons may come from an optically thick accretion disc or clouds in the vicinity of the hot plasma, or may be internally produced by the synchrotron process (see e.g. Xie et al. 2010). For example, non-simultaneous data for the Seyfert NGC 5548 from *ROSAT*, *Ginga* and *CGRO/OSSE* have yielded the plasma temperature, $kT_e \simeq 55$ keV, and the Thomson optical depth, $\tau \simeq 2$ (Magdziarz et al. 1998). The average OSSE spectra of 11 Sy 1s

[★]Based on observations with *INTEGRAL*, an ESA project with instruments and science data centre funded by ESA member states (especially the PI countries: Denmark, France, Germany, Italy, Switzerland and Spain), the Czech Republic and Poland and with participation of Russia and the US.
†E-mail: lubinski@ncac.torun.pl (PL); aaz@camk.edu.pl (AAZ)

and eight Sy 2s have yielded similar parameters, $kT_e \simeq 70\text{--}80$ keV, $\tau \simeq 1.7$ (Zdziarski, Poutanen & Johnson 2000). On the other hand, Petrucci et al. (2000) obtained a much higher $kT_e \simeq 250$ keV (and $\tau \simeq 0.2\text{--}0.4$) for NGC 5548 using *BeppoSAX* data and a different anisotropic Comptonization model in the slab geometry. Then, Petrucci et al. (2001a, hereafter P01) found, with the same model, a similarly high values of $kT_e \simeq 170\text{--}320$ keV (and $\tau \simeq 0.05\text{--}0.20$) for six Sy 1s observed by *BeppoSAX*. We note, however, that such high kT_e yield spectra being well above the OSSE fluxes at $\gtrsim 100$ keV for NGC 5548, NGC 4151 and other Seyferts.

The nearby, $z = 0.0033$, Seyfert 1.5 galaxy NGC 4151 is the second (after Cen A) brightest persistent active galactic nuclei (AGN) in the 20–100 keV band. Its electromagnetic spectrum has been extensively studied, with its properties in the radio, infrared, optical, ultraviolet and X γ bands well established. Its black hole mass has been estimated based on reverberation as $(4.6^{+0.6}_{-0.5}) \times 10^7 M_\odot$ (Bentz et al. 2006). Although this estimate is subject to a systematic uncertainty by a factor of $\sim 3\text{--}4$, it is consistent with the estimate based on scaling of the power spectrum to Cyg X-1 of Czerny et al. (2001). The overall picture of the region surrounding the nucleus, based on *Hubble Space Telescope* (*HST*)/*STIS*, *Chandra* and *XMM-Newton* data, is that the complex absorption observed for NGC 4151 is due to massive outflows, presumably disc winds, forming several regions characterized by a range of column densities, N_H , and ionization levels (Schurch et al. 2004; Kraemer et al. 2006). This explains earlier results from *ROSAT*, *ASCA*, *Ginga* and *RXTE* satellites, with the medium-energy X-ray spectra fitted only after applying a complex absorber model, consisting of several components fully and partially covering the central source (e.g. Zdziarski, Johnson & Magdziarz 1996a; Zdziarski et al. 2002, hereafter Z02). The absorber undergoes rapid daily changes of N_H (Puccetti et al. 2007). Also, a narrow Fe $K\alpha$ line with the equivalent width of 50–200 eV is observed (Z02; Schurch et al. 2003; De Rosa et al. 2007).

NGC 4151 has frequently been observed by *CGRO* and *BeppoSAX*. The e-folded power-law model yields $E_c \simeq 50\text{--}200$ keV (Johnson et al. 1997; De Rosa et al. 2007). Thermal Compton models yield $kT_e \simeq 50\text{--}80$ keV, $\tau \simeq 1\text{--}2$ (Johnson et al. 1997; Z02). The strength of Compton reflection is moderate, $R \approx 0.4$ (e.g. De Rosa et al. 2007).

NGC 4151 was observed by *INTEGRAL* eight times as a primary or secondary target. The results of the first dedicated observation of 2003 May are given in Beckmann et al. (2005). The object was found in a spectral state similar to those observed with OSSE, but at the highest flux level ever noticed. There was no significant spectral variability despite ~ 50 per cent variations of the flux. A thermal Compton model fitted to the summed spectrum yielded $kT_e \simeq 90$ keV, $\tau \simeq 1.3$, $R \simeq 0.7$, $N_H \simeq 7 \times 10^{22}$ cm $^{-2}$. During almost all later *INTEGRAL* observations the source was found at moderate to very low flux levels. This has allowed us to study the spectral properties of the dim state of this AGN with unprecedented precision and compare them with the bright state of 2003 May.

2 OBSERVATIONS AND DATA REDUCTION

We use all NGC 4151 data collected by *INTEGRAL* as of 2010 January (see Table 1). Good quality data come from the dedicated NGC 4151 observations made in 2003 May, 2007 January, May and December, and 2008 May. The remaining data are taken from observations of the Coma cluster, Mrk 273, NGC 4736, M51 and Mrk 421, when NGC 4151 was almost always seen at an off-axis angle of $9^\circ\text{--}15^\circ$. We select the data with the off-axis angle $< 15^\circ$ for ISGRI and SPI, and $< 3^\circ$ for the JEM-X and OMC. The data have been

reduced using the Offline Scientific Analysis (osa) 7.0 provided by the *INTEGRAL* Science Data Centre (Courvoisier et al. 2003), with the pipeline parameters set to the default values. Since the osa v. 8.0 of 2009 August brought a major improvement to the JEM-X data analysis, we have used it for these data. The ISGRI and SPI spectra and light curves have been extracted with the standard spectral extraction software, including the catalogue sources NGC 4151, NGC 4051, NGC 4138, Mrk 766, NGC 4258, NGC 4395, Coma Cluster, NGC 5033, Mrk 421 and Mrk 268. The JEM-X spectra have been obtained from mosaic images stacked for a given observation. We use the standard response files for all instruments. The OMC magnitude was converted into flux using the calibration of Johnson (1966), $F(V = 0) = 3.92 \times 10^{-9}$ erg cm $^{-2}$ s $^{-1}$ Å $^{-1}$.

To better constrain the spectra at low energies, we supplemented the *INTEGRAL* data by all available X-ray observations of NGC 4151 taken since 2003 by *RXTE*, *XMM-Newton* and *Suzaku* (see Table 2). The *RXTE* PCU2 light curves and spectra and HEXTE spectra were extracted with the HEASOFT 6.5.1, using the standard selection criteria. The five *XMM-Newton* observations (denoted here as X1–X5) were analyzed with SAS 8.0.1. We used only the EPIC pn data, and excluded periods of high or unstable background. The spectra X1 and X2 have been found to be compatible with each other; we have therefore added them together. For the single *Suzaku* observation, the data in the 3×3 mode were reduced with HEASOFT 6.6. The spectra of the front-illuminated CCD, XIS0 and XIS3 were added together, whereas the spectrum of the back-illuminated detector XIS1 was used separately. We also extracted the HXD/PIN spectrum using the standard procedure. Although there have been a number of *Chandra* NGC 4151 observations, all those without gratings that were public at the time we started the analysis were from before 2000 March.

Tables 1 and 2 identify the data used for our three main spectral sets, bright (B), medium (M) and dim (D), whose selection is based on ISGRI flux. The remaining *INTEGRAL* data, not marked with a letter in Table 1, were not used for the spectral analysis. We have excluded them because either there were no corresponding high-quality spectra from other X-ray satellites (e.g. Revs. 0809–0811) and/or their flux level was outside the range assumed by us (e.g. beginning of Rev. 0074 and Rev. 0076 in the case of the B state). The data sets from the other satellites were not always simultaneous with the *INTEGRAL* data. Thus, we assign them to one of the three sets based again on the flux, using the monitoring data from *Swift*/BAT (see Sections 3 and 4.1 for details of the selection).

3 VARIABILITY

NGC 4151 is being observed with X γ detectors for almost 40 yr. The satellite and balloon results up to 1988 were compiled by Perotti et al. (1991). Then, it has been observed above 20 keV by *Ginga*, *GRANAT*, *CGRO*, *BeppoSAX*, *INTEGRAL*, *Swift* and *Suzaku*. Fig. 1(a) shows the 20–100 keV flux observed since 1972 October compared to the optical flux and the *RXTE*/ASM count rate. Because the spectra from earlier observations are not publicly available, the 20–100 keV fluxes were determined using the values of the flux at 35 keV and of the photon index presented in table 2 of Perotti et al. (1991). For this reason, we do not show their uncertainties. Similarly, the *GRANAT* fluxes were determined using table 3(a) of Finoguenov et al. (1995), where the ART-P and SIGMA spectra are fitted by a power-law model. For all other observations, we use the spectra from HEASARC (*CGRO*/OSSE, *BeppoSAX*/PDS) or spectra extracted by us (*INTEGRAL*/ISGRI, *Suzaku*/PIN), where the

Table 1. The observation log of *INTEGRAL*. The ISGRI exposure is effective, corresponding to fully coded observations, and the JEM-X one is summed over all pointings with the off-axis angle $<3^\circ$. The last column gives the spectral set as defined in Section 4.1; B = bright, D = dim, M = medium.

Revolution	Start time, UTC (MJD)	End time, UTC (MJD)	Eff. exposure (s)	JEM-X exposure (s)	Spectral set
0036	2003-01-29 16:43 (52668.697)	2003-01-31 08:18 (52670.346)	11296	–	–
0071	2003-05-14 12:42 (52773.529)	2003-05-16 11:39 (52775.485)	9908	–	–
0072	2003-05-17 13:22 (52776.557)	2003-05-18 19:56 (52777.831)	5376	–	–
0073	2003-05-20 18:44 (52779.781)	2003-05-22 10:23 (52781.433)	20441	–	–
0074	2003-05-23 08:35 (52782.358)	2003-05-25 11:42 (52784.488)	117528	91633	B
0075	2003-05-25 21:03 (52784.877)	2003-05-28 05:33 (52787.231)	153481	153481	B
0076	2003-05-28 20:51 (52787.869)	2003-05-29 12:13 (52788.509)	39533	39533	–
0274	2005-01-10 16:05 (53380.670)	2005-01-12 17:36 (53382.733)	9146	–	–
0275	2005-01-13 19:36 (53383.817)	2005-01-15 04:20 (53385.181)	11745	–	–
0310	2005-04-29 16:32 (53489.689)	2005-04-30 03:46 (53490.157)	1734	–	D
0311	2005-05-01 08:54 (53491.371)	2005-05-02 20:28 (53492.853)	3290	–	D
0312	2005-05-03 22:44 (53493.947)	2005-05-04 09:57 (53494.416)	1062	–	D
0317	2005-05-19 18:04 (53509.753)	2005-05-21 01:09 (53511.048)	10144	–	D
0318	2005-05-22 01:03 (53512.044)	2005-05-24 06:37 (53514.276)	7894	–	D
0324	2005-06-09 17:55 (53530.747)	2005-06-10 23:12 (53531.967)	9748	–	D
0448	2006-06-14 09:54 (53900.413)	2006-06-17 00:03 (53903.002)	29525	–	D
0449	2006-06-17 10:19 (53903.430)	2006-06-19 23:47 (53905.991)	28497	–	D
0450	2006-06-20 09:23 (53906.391)	2006-06-22 23:29 (53908.978)	26974	–	D
0451	2006-06-23 09:06 (53909.379)	2006-06-25 23:10 (53911.965)	26844	–	D
0521	2007-01-18 16:45 (54118.698)	2007-01-20 23:28 (54120.978)	122878	122878	D
0522	2007-01-21 16:35 (54121.691)	2007-01-24 06:07 (54124.255)	123751	105848	D
0561	2007-05-18 09:31 (54238.397)	2007-05-20 16:11 (54240.674)	110696	110696	D
0562	2007-05-22 00:44 (54242.031)	2007-05-23 21:34 (54243.899)	100729	78177	D
0563	2007-05-24 09:06 (54244.379)	2007-05-25 06:31 (54245.272)	46903	46903	D
0634	2007-12-22 17:53 (54456.745)	2007-12-25 07:19 (54459.305)	131811	131811	M
0636	2007-12-28 17:26 (54462.726)	2007-12-31 01:53 (54465.078)	119738	100028	M
0678	2008-05-02 21:17 (54588.887)	2008-05-04 22:36 (54590.942)	24805	–	M
0679	2008-05-05 20:47 (54591.866)	2008-05-07 07:09 (54593.298)	17266	–	M
0809	2009-05-31 11:31 (54982.480)	2009-05-31 20:58 (54982.874)	20019	2891	–
0810	2009-06-01 05:49 (54983.242)	2009-06-03 16:10 (54985.674)	112086	46546	–
0811	2009-06-04 05:37 (54986.234)	2009-06-06 10:24 (54988.433)	108501	40239	–

Table 2. The observation log for the other X-ray satellites. The exposure times are given for the *RXTE* PCU2 (where the number of pointings added together is shown in parentheses), EPIC pn (*XMM-Newton*) and XIS (*Suzaku*) detectors. The last column shows the data set as defined in Table 1, and, in the case of *XMM-Newton*, its consecutive observation number.

Obs. ID	Start time, UTC (MJD)	End time, UTC (MJD)	Exposure	Spectral set
<i>RXTE</i>				
80416-01-01-(00–09)	2003-05-24 05:49 (52783.242)	2003-05-29 04:18 (52788.179)	15760 (11)	B
92113-08-(06–09)	2006-05-13 02:28 (53868.103)	2006-06-23 15:42 (53909.654)	4240 (4)	D
92113-08-(22–35)	2006-12-23 12:51 (54092.535)	2007-06-22 08:57 (54273.373)	14272 (14)	D
<i>XMM-Newton</i>				
0143500101	2003-05-25 01:38 (52784.068)	2003-05-25 06:54 (52784.288)	5821	X1, B
0143500201	2003-05-26 20:35 (52785.858)	2003-05-27 01:51 (52786.077)	11389	X2, B
0143500301	2003-05-27 15:17 (52786.637)	2003-05-27 20:33 (52786.856)	12291	X3, B
0402660101	2006-05-16 06:22 (53871.265)	2006-05-16 17:35 (53871.733)	27980	X4, D
0402660201	2006-11-29 17:20 (54068.722)	2006-11-30 08:00 (54069.333)	21468	X5, M
<i>Suzaku</i>				
701034010	2006-12-18 20:05 (54087.837)	2006-12-21 09:14 (54090.385)	124980	D

20–100 keV flux was computed from a power-law model fit (which was done in the 50–150 keV range for the OSSE data) and the uncertainty was determined from the relative error of the summed count rate in the fitted band. Fig. 1(b) shows the 20–100 keV fluxes from the *CGRO/BATSE* in 7-d bins (together with those from OSSE). They have been obtained from the 20–70 keV fluxes given by Parsons et al. (1998) by multiplying by 1.1 (assuming $\Gamma = 1.8$)

and then dividing by the normalization factor with respect to OSSE of 1.42 (Parsons et al. 1998).

Fig. 1(b) gives the 1.5–12 keV count rate of *RXTE*/ASM¹ in 30-d bins. The blue curve in Fig. 1(c) shows the optical data

¹<http://xte.mit.edu/asmlc/ASM.html>

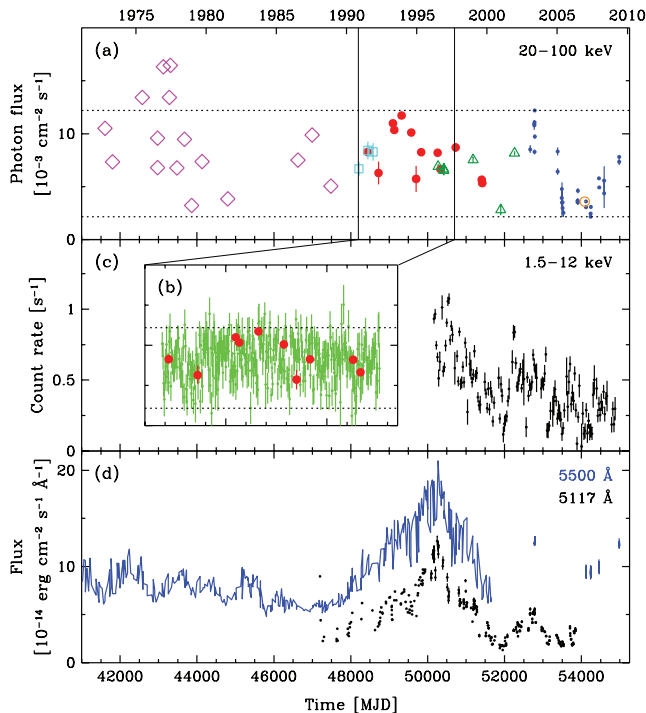


Figure 1. Light curves of NGC 4151 since 1972. (a) The 20–100 keV flux from the compilation by Perotti et al. (1991), magenta diamonds, and from *GRANAT*/SIGMA (cyan squares), from *CGRO*/OSSE (red filled circles), from *BeppoSAX*/PDS (green triangles), from *INTEGRAL*/ISGRI (blue dots) and from *Suzaku*/PIN (the orange open circle). The dotted lines show the extrema of the 20–100 keV flux from ISGRI. (b) The 20–100 keV flux from *CGRO*/BATSE (green error bars) together with that from OSSE (red filled circles); the same as in a). (c) The *RXTE*/ASM count rate in 30-d bins. (d) The 5500 Å flux (Czerny et al. 2003, blue lines), and from *INTEGRAL*/OMC (vertical blue bars at MJD > 52000), and the 5117 Å flux (Shapovalova et al. 2008, black dots).

from the Crimean observatory in the *V* band (5500 Å; Czerny et al. 2003), which, after MJD 52000, are supplemented by the *INTEGRAL*/OMC data. Since the *V*-band data do not overlap much in time with the ASM data, we also show the 5117 Å fluxes from various observatories given by Shapovalova et al. (2008).

The 1.5–12 keV count rate appears well correlated with the optical fluxes (see Fig. 1). As found by Czerny et al. (2003), the medium-energy X-ray flux of NGC 4151 varies on time-scales $\sim 5\text{--}10^3$ d, whereas the optical variability is also present on longer time-scales. For hard X-rays, a correlation with the optical and the 1.5–12 keV fluxes is less clear. The main peak of the optical emission at MJD $\simeq 49000\text{--}51000$ (1993–1998) is reflected in the 1.5–12 keV flux but not in the 20–100 keV one (including the BATSE data). The later data from *BeppoSAX*, *INTEGRAL* and *Suzaku* show an overall agreement with the optical and softer X-ray fluxes in a sense that the minima at MJD ~ 52000 and MJD ~ 54000 and the maximum at MJD ~ 52800 appear for all these bands. However, the scarce hard X-ray coverage prevents unambiguous conclusions.

The results shown in Figs 1(a) and (b) show that the hard X-ray emission of NGC 4151 has varied in well-defined limits over the last 39 yr. Almost all fluxes are within the extreme 20–100 keV fluxes from ISGRI (with the maximum in 2003 May and the minimum in 2007 May). There are four flux measurements from older (1975–77) observations above this maximum. However, they are relatively doubtful, corresponding to marginal ($\approx 2\text{--}3\sigma$) detections

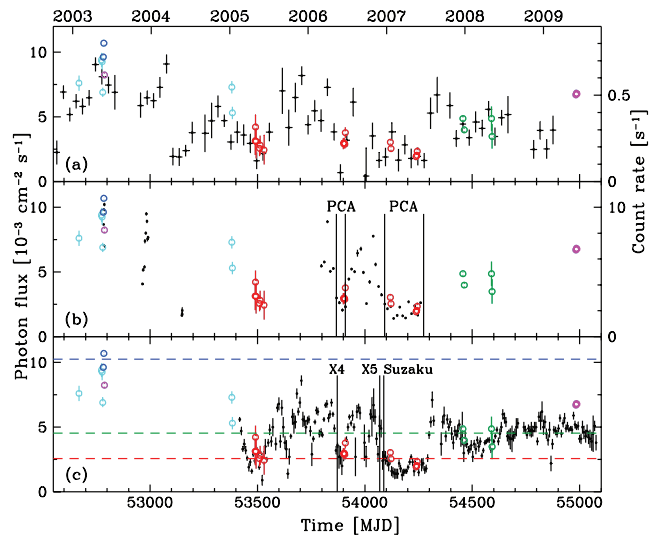


Figure 2. Medium and hard X-ray light curves from *INTEGRAL*/ISGRI compared to those from *RXTE* and *Swift* (shown with black circles and error bars). The 18–50 keV ISGRI flux is shown by open circles on all panels. The colours identify the three main states, bright (blue), medium (green), dim (red) and, additionally, data excluded from the spectral analysis, Revs. 0076 and 0809–0811 (magenta), and the rest (cyan). (a) The *RXTE*/ASM count rate in 30-d bins (right axis). (b) The *RXTE*/PCU2 count rate (right axis). The vertical lines delineate the two periods for which the dim state PCA spectrum was obtained. (c) Comparison with the *Swift*/BAT 15–50 keV flux in 7-d bins. The vertical lines show the times of the X4 (dim), X5 (medium) *XMM-Newton* observations and that of *Suzaku* (dim). The horizontal dashed lines show the average flux levels of ISGRI bright, medium and dim states.

at $\gtrsim 40$ keV. Thus, ISGRI 20–100 keV flux range appears very close to the corresponding overall actual range. This is also supported by the BATSE data (Fig. 1b), varying within this range. We also notice that NGC 4151 was rarely seen at low hard X-ray fluxes before the *INTEGRAL* launch.

Fig. 2 compares ISGRI 18–50 keV fluxes with the contemporaneous data in the medium and hard X-ray bands from *RXTE* and *Swift*. The ISGRI fluxes are well correlated with those from both *RXTE* and the *Swift*/BAT.² In particular, we see a good correlation with the 1.5–12 keV rate in spite of the variable absorption affecting a lower part of this band. Fig. 2 also shows that a large fraction of the *INTEGRAL* observations took place during periods with very low hard X-ray flux. Fig. 2 also identifies the *INTEGRAL* observations used for the spectral sets (Table 1).

The BAT light curve (Fig. 2c) shows that the hard X-ray flux varies by a factor of a few on a week time-scale. When the source is sufficiently bright, it is possible for ISGRI to monitor hour time-scale variability. This was the case for the bright state of 2003 May, and the source showed such variability (see Fig. 3). The shown ISGRI and OMC light curves were extracted with a time bin equal to a single pointing duration (10 m–2.5 h, typically ~ 1 h). When observed in dimmer states, ISGRI flux remains constant within the measurement errors during a given continuous observation. The optical flux appears constant on hour–day time-scales. Still, it varies on longer time-scales, and it increases by ~ 30 per cent when the source is bright in X-rays (2003 May, 2009 June).

² <http://swift.gsfc.nasa.gov/docs/swift/results/transients>

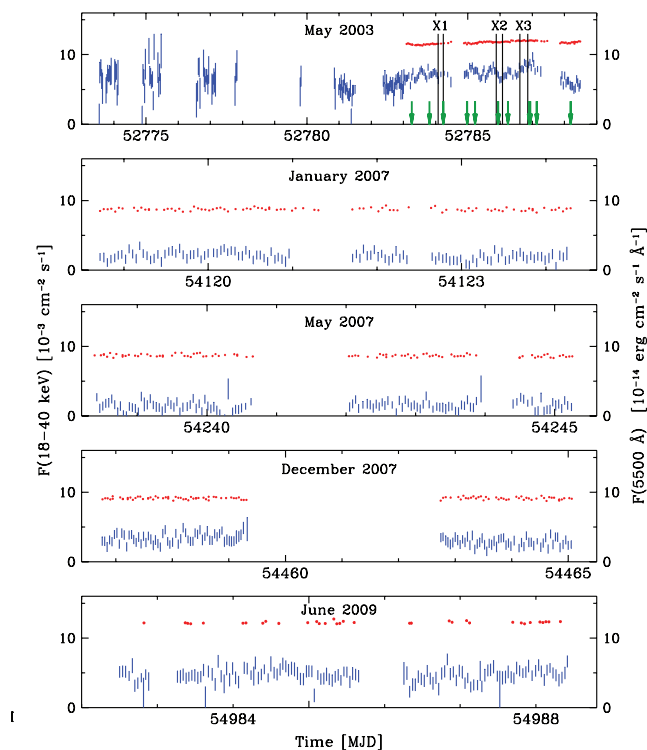


Figure 3. Illustration of short time-scale variability. The blue bars (left axis) and the red dots show the 18–40 keV ISGRI flux and the optical OMC flux, respectively, during the dedicated *INTEGRAL* observations. The vertical lines and the green arrows in the top panel show the times of the bright-state X1–X3 *XMM-Newton* and 11 *RXTE/PCA* observations, respectively. The data used for the bright *INTEGRAL* spectrum are those in the top panel simultaneous with the OMC observations except those around MJD 52788 (Rev. 0076), which have markedly lower fluxes.

We have extracted the bright (X1–X3) *XMM-Newton*/EPIC pn light curves in several energy bands in 100-s time bins, and compared with the OMC 100-s light curves. No variability is seen in either light curves on time-scales $\lesssim 1$ h. The *XMM-Newton* light curves vary slowly in good agreement with the trends observed for ISGRI (and also JEM-X) fluxes.

The *INTEGRAL* data are suitable for correlation studies because they provide simultaneous data in the optical, medium and hard X-ray bands. Here, we use all the observations with the off-axis angle $< 3^\circ$ for which OMC and JEM-X data are available. They also include part of the observations not used in our spectral analysis, namely those identified with magenta circles in Fig. 2. Fig. 4 shows the correlations between the 18 and 40 keV flux and those fluxes in the 3–10 keV and *V* bands. Both show strong correlations, but the correlation patterns are different. The optical fluxes fall into two separate regions, within each they are correlated with the hard X-rays. Significant rank-order probabilities (> 0.999) of the ISGRI/OMC correlation are found separately not only for each of the regions, but also for the entire data set. The observed bimodality may result from strong optical long-term variability between the X-ray observations. On the other hand, the 3–10 keV and 18–40 keV fluxes exhibit a single, extremely strong, linear correlation. Statistical uncertainty blurs somewhat the correlation for low fluxes. This result indicates that during all *INTEGRAL* observations the slope of the X-ray spectrum of NGC 4151 below 40 keV remains approximately constant.

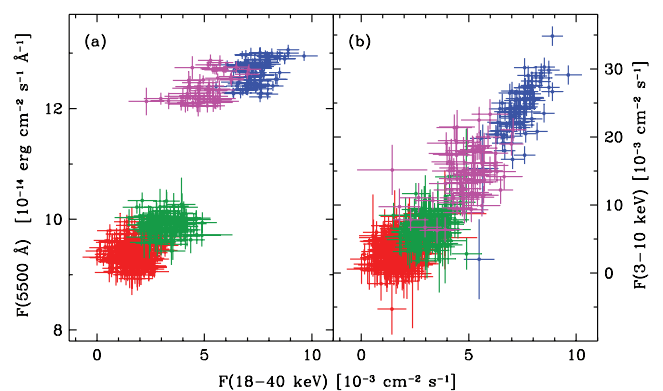


Figure 4. (a) The OMC 5500 Å flux versus the ISGRI 18–40 keV flux. (b) The JEM-X 3–10 keV flux versus the ISGRI flux. Each cross corresponds to a single *INTEGRAL* pointing. The colours identify the three main states, bright (blue), medium (green), dim (red), and, additionally, Revs. 0076, 0809–0811 (magenta).

4 SPECTRAL ANALYSIS

4.1 Assumptions and selection of spectral sets

Spectral fitting is performed with *XSPEC* 11.3 (Arnaud 1996). Errors are given for 90 per cent confidence level for a single parameter, $\Delta\chi^2 = 2.7$. The luminosity and distance, $D = 13.2$ Mpc, are for $H_0 = 75$ km s $^{-1}$ Mpc $^{-1}$. We use the elemental abundances of Anders & Ebihara (1982) and the photoelectric absorption cross-sections from Bałucińska-Church & McCammon (1992). The Galactic column density is set to $N_{\text{H}}^{\text{G}} = 2.1 \times 10^{20}$ cm $^{-2}$. The assumed inclination angle of the reflector and the hot plasma (for anisotropic geometries) is $i = 45^\circ$ (Das et al. 2005). The reflector is assumed to be neutral, and relativistic broadening of reflected spectra is neglected. Still, in some cases we test for the effects of either a variable Fe abundance of the intrinsic absorber and the reflector, a variable i , or an ionization of the reflector.

The main assumption used in our selection of spectral sets is that the state of the emitting hot plasma is determined by the hard X-ray flux. This is justified by our finding that the shape of ISGRI spectra for a given revolution is almost constant at a given hard X-ray flux. As an additional constraint, we do not split *INTEGRAL* data from a single revolution into different spectral sets. Based on this criterion, we select three average ISGRI spectra, as specified in Table 1 and Fig. 2. These spectra are accompanied by spectra taken with the other instruments. The state is assigned to each of them on the basis of the light curves presented in Figs 2 and 3. In particular, the high quality of the *Swift*/BAT data allows us to determine the hard X-ray flux for periods with no *INTEGRAL* observations, and thus to assign the correct state to the existing lower-energy data sets (Table 2). On the other hand, the data from *RXTE* determine by themselves the hard X-ray state.

The ISGRI bright (B) and dim (D) spectra are of relatively good quality, and correspond to the extrema of the measured hard X-ray flux. For the flux range in between, we identify two flux ranges. However, we had no corresponding low-energy data sets for the upper of them. Thus, we use the lower of them, denoted as medium (M). The fitted data sets are as follows.

The bright state, B. We use the data from 2003 May made at low off-axis angles, as shown in the top panel of Fig. 3. The spectrum includes a part of Rev. 0074 (without its beginning) and Rev. 0075. For these data, we have simultaneous *RXTE* and *XMM-Newton* observations (see Table 2). The fitted spectral set consists of ISGRI

spectrum, the X1+X2 and X3 *XMM–Newton* spectra, and the *RXTE* PCU2 spectrum summed over 11 observations.

The medium state, M. We sum ISGR1 data from Revs. 0634, 0636, 0678–0679, and use the summed JEM–X 1 spectrum from Revs. 0634 and 0636, and the X5 *XMM–Newton* spectrum.

The dim state, D. The summed ISGR1 spectrum is from Revs. 0310–0563. We use the *RXTE* PCU2, the X4 *XMM–Newton* EPIC pn, and the *Suzaku* XIS0,3 and XIS1 spectra.

We have also investigated the effect of including other available spectra for each of the data set, whose resulting sets we denote as ‘extended’. The extended set B also includes the spectra from the *INTEGRAL*/JEM–X 2 and SPI, and the *RXTE*/HEXTE clusters 0, 1. The extended set M also includes the SPI spectrum. The extended data set D also includes two *INTEGRAL* JEM–X 1 summed spectra, from Revs. 0521–0522 and 0561–0563, the *Suzaku* PIN spectrum, the *RXTE* HEXTE cluster 1 spectrum and the corresponding SPI spectrum. We discuss the effect of using the extended data sets in Section 4.3.

In order to limit the complexity of the fitted models, we have decided not to use the X-ray spectra at $E < 2.5$ keV. A two-component partial absorption was then sufficient to model absorption of the continuum. Using the X-ray spectra in the 0.1–2.5 keV band would have required to add a number of spectral lines as well as a soft excess component. As we have tested, including that low-energy band would not affect our determination of the parameters of the hot plasma and of Compton reflection.

Thus, the EPIC pn, XIS0+XIS3 and XIS1 spectra were used in the 2.5–11.3, 2.5–9.5 and 2.5–9.0 keV bands, respectively. The PCA/PCU2 and JEM–X spectra were fitted in the 3–16 and 4–19 keV bands, respectively. The HXD/PIN spectrum was used in the 19–60 keV band because the <19 keV data were showing a strong excess. For ISGR1, data below 20 keV were always excluded, whereas the high-energy limit was in the 180–200 keV range, depending on our 3σ detection threshold used to select good spectral channels. The ISGR1 spectra in the staring mode from Revs. 0074 to 75 show an excess of ~ 10 per cent below 23 keV, whose origin remains unknown. It could be related to a specific setting of the low-energy threshold in the early period of the mission. Thus, we used only the data at > 23 keV in this case. The HEXTE spectra were used in the 13–160 keV band for the bright state and in 23–110 keV for the dim state. The SPI spectra were fitted in the 23–200 keV band.

While fitting a given spectral set, the parameters of intrinsic continua are the same for all included spectral data, allowing only the normalization of the model to vary between them. This reflects our assumption that the hard X-ray flux determines the intrinsic state of the source, even for non-simultaneous data. On the other hand, absorption and the Fe K emission may vary quickly (Puccetti et al. 2007), and we cannot expect their parameters to be the same for different low-energy spectra associated with the same spectral set. Thus, we have allowed them to vary between different spectra. Our assumed absorber consists of one fully covering the source with the column density of N_{H}^{p} , and the ionization parameter, $\xi \equiv 4\pi F_{\text{i}}/n$, where F_{i} is the 5 eV–20 keV irradiating flux and n is the density of the reflector. For the low-resolution detectors, PCA and JEM–X, we assumed $\xi = 0$. For the high-resolution detectors, EPIC pn and XIS, we allowed $\xi > 0$, and, in addition, we included partial-covering neutral absorption, with the column density of N_{H}^{p} covering a fraction of f^{p} of the flux. For the ionized absorption, we use the model by Done et al. (1992). Although it is not applicable to highly ionized plasma, it is sufficiently accurate at low/moderate ionization, such as that found in our data. Absorption for ISGR1, HEXTE, SPI and PIN spectra is only marginally important, and we

Table 3. Spectral fitting results for the e-folded power-law model including reflection. The *xSPEC* model is `CONSTANT*WABS*ABSORI*ZPCFABS(PEXRAV + ZGAUSS)`, and the normalization, K , is given by the photon flux at 1 keV in units of 10^{-2} keV $^{-1}$ cm $^{-2}$ s $^{-1}$.

State	E_{c} (keV)	Γ	R	K	$\chi^2/\text{d.o.f.}$
Bright	264^{+48}_{-26}	$1.71^{+0.06}_{-0.01}$	$0.45^{+0.12}_{-0.05}$	$8.7^{+1.1}_{-0.3}$	3179/3414
Medium	> 1025	$1.81^{+0.05}_{-0.03}$	$0.6^{+0.3}_{-0.3}$	$4.6^{+1.4}_{-0.7}$	1554/1599
Dim	> 1325	$1.81^{+0.01}_{-0.01}$	$0.92^{+0.05}_{-0.05}$	$2.24^{+0.01}_{-0.02}$	3338/3384

thus used only the neutral fully covering N_{H}^{p} at the values fitted to the corresponding PCA or JEM–X spectra. The Fe K α emission is modelled by a Gaussian line, with the centre energy, width, photon flux and equivalent width of E_{Fe} , σ_{Fe} , I_{Fe} and w_{Fe} , respectively. Fitting the dim state spectra, we have found that adding an Fe K β line (at ≈ 7.1 keV) was significantly improving the fit for the EPIC pn and XIS spectra.

4.2 The cut-off power-law model

We first fit an e-folded power-law model including a Compton reflection component. This allows us to compare our results to other published ones. We use the *PEXRAV* model (Magdziarz & Zdziarski 1995), and our other assumptions are specified above. The results are shown in Table 3, where we do not show the fitted absorber and line parameters since they are similar to those for our main model of thermal Comptonization (see Section 4.3).

Our results regarding Γ and R are similar to those of earlier works. However, a significant difference is found for the e-folding energy, E_{c} , which we find to be high, and compatible with no cut-off for two of our states (see Table 3). A finite E_{c} is found only for the bright state. Even then, we obtain values well above those reported before, which are 30–45 keV (P01), 80–180 keV (De Rosa et al. 2007) and ~ 210 keV (Z02). As discussed in Zdziarski et al. (2003), an exponential cut-off is much shallower than that characteristic of thermal Comptonization, and not sharp enough to model the spectral high-energy cut-offs observed in Seyferts, in particular in NGC 4151. Thus, our high values of E_{c} result from the good quality of the data below the cut-off, which dominate the statistics and force an approximately straight power law to continue to just below the beginning of the cut-off.

4.3 Comptonization model

To model thermal Comptonization, we use the *COMPBS* model (Poutanen & Svensson 1996) in *xSPEC*. It models Compton scattering in a plasma cloud of given temperature, T_{e} , and Thomson optical depth, τ , for a number of geometries and locations of the seed photon sources. Since T_{e} and τ are strongly intrinsically anticorrelated, we also use the Compton parameter (e.g. Rybicki & Lightman 1979), $y \equiv 4(kT_{\text{e}}/m_{\text{e}}c^2)\tau$ (where m_{e} is the electron mass), as the second fitting parameter instead of τ . The advantage of this choice is that T_{e} and y are almost orthogonal; y determines closely the power-law slope at low energies whereas kT_{e} determines the position of the high-energy cut-off. The seed photons are assumed to have a disc blackbody distribution (*DISKBB* in *xSPEC*; Mitsuda et al. 2004) with the maximum temperature of $kT_{\text{bb}} = 10$ eV. The model normalization, K , is that of the seed disc blackbody model as defined in *xSPEC* (see Section 5.3).

Among the geometries included in *COMPBS*, we consider here four spherical cases; an approximate treatment of radiative transfer

using escape probability (which is denoted in COMPPS by the geometry parameter = 0), a sphere with central soft photons (geometry 4), homogeneously distributed seed photons (geometry -4) and seed photons distributed according to the diffusion-equation eigenfunction, $\propto \sin(\pi\tau'/\tau)/(\pi\tau'/\tau)$, where $0 \leq \tau' \leq \tau$ (-5). Then, we consider a slab with the seed photons either at its bottom (geometry 1) or distributed homogeneously (geometry -1). Also, we consider the hot plasma in the shape of either a cylinder, with the height equal to its radius, or a hemisphere, with the seed photons being either at its bottom (2, 3, respectively) or homogeneously distributed (-2, -3, respectively).

The spectral data of NGC 4151 studied in this paper are of high quality and represent the largest set ever collected for this source. This gives us a possibility to test how precise information about X γ emission from brightest Seyferts can be achieved with the current satellites. Therefore, we extensively test various variants of the Comptonization model for our two best-quality states, bright and dim. This could, in principle, give us some indications regarding the actual geometry of the source. Our results are presented in Tables 4(a) and (b), regarding the parameters of the Comptonizing plasma and the strength of reflection (which are the same for all used detectors within a given state), and of the absorber and the Fe

Table 4(a). Spectral fitting results with thermal Comptonization as the main continuum. The XSPEC model is `CONSTANT*WABS*ABSORI*ZPCFABS*(COMPPS + ZGAUSS)`. See Section 4.3 for the definitions of the parameters. $L_{X\gamma}$ and $L'_{X\gamma}$ are the bolometric model luminosity (in units of 10^{43} erg s $^{-1}$) with and without the reflection component, respectively, and only the values for the geometry 0 are given as the values for other geometries are similar.

State	kT_e (keV)	y	τ	R	$K(10^8)$	$L_{X\gamma}$	$L'_{X\gamma}$	Geometry	$\chi^2/\text{d.o.f.}$
Bright	54^{+7}_{-5}	$1.10^{+0.02}_{-0.02}$	$2.6^{+0.3}_{-0.3}$	$0.40^{+0.07}_{-0.06}$	$5.2^{+1.4}_{-0.6}$	5.18	4.61	Sphere (0)	3165/3414
	62^{+7}_{-7}	$0.60^{+0.01}_{-0.01}$	$1.3^{+0.1}_{-0.1}$	$0.55^{+0.08}_{-0.07}$	$7.3^{+1.9}_{-0.9}$			Slab (1)	3166/3414
	62^{+9}_{-7}	$0.61^{+0.01}_{-0.01}$	$1.3^{+0.1}_{-0.2}$	$0.55^{+0.09}_{-0.06}$	$3.9^{+0.4}_{-0.7}$			Slab (-1)	3166/3414
	73^{+14}_{-9}	$1.06^{+0.02}_{-0.02}$	$1.9^{+0.4}_{-0.2}$	$0.47^{+0.05}_{-0.07}$	$12.0^{+2.9}_{-1.6}$			Cylinder (2)	3168/3414
	73^{+13}_{-13}	$1.06^{+0.03}_{-0.01}$	$1.9^{+0.3}_{-0.3}$	$0.51^{+0.5}_{-0.9}$	$5.4^{+1.4}_{-1.1}$			Cylinder (-2)	3168/3414
	73^{+16}_{-7}	$1.21^{+0.02}_{-0.02}$	$2.1^{+0.4}_{-0.6}$	$0.48^{+0.06}_{-0.06}$	$11.9^{+3.2}_{-1.4}$			Hemisphere (3)	3168/3414
	73^{+15}_{-9}	$1.21^{+0.03}_{-0.02}$	$2.1^{+0.3}_{-0.4}$	$0.50^{+0.08}_{-0.06}$	$4.7^{+1.5}_{-1.0}$			Hemisphere (-3)	3168/3414
	61^{+7}_{-5}	$0.80^{+0.01}_{-0.02}$	$1.7^{+0.1}_{-0.2}$	$0.38^{+0.04}_{-0.05}$	$1.2^{+0.1}_{-0.1}$			Sphere (4)	3172/3414
	57^{+13}_{-7}	$0.86^{+0.01}_{-0.01}$	$1.9^{+0.2}_{-0.4}$	$0.39^{+0.06}_{-0.05}$	$6.4^{+0.6}_{-0.6}$			Sphere (-4)	3169/3414
	57^{+10}_{-5}	$0.86^{+0.01}_{-0.01}$	$1.9^{+0.2}_{-0.3}$	$0.38^{+0.06}_{-0.05}$	$4.9^{+1.5}_{-0.4}$			Sphere (-5)	3166/3414
Medium	128^{+74}_{-24}	$1.02^{+0.08}_{-0.13}$	$1.0^{+0.5}_{-0.3}$	< 0.41	$3.9^{+0.4}_{-1.0}$	2.26	2.16	Sphere (0)	1554/1597
Dim	190^{+13}_{-12}	$0.98^{+0.01}_{-0.01}$	$0.66^{+0.04}_{-0.05}$	$0.75^{+0.04}_{-0.04}$	$1.54^{+0.01}_{-0.01}$	1.47	1.19	Sphere (0)	3337/3384
	200^{+7}_{-8}	$0.49^{+0.01}_{-0.01}$	$0.31^{+0.01}_{-0.01}$	$1.01^{+0.05}_{-0.05}$	$2.04^{+0.01}_{-0.02}$			Slab (1)	3335/3384
	188^{+6}_{-7}	$0.48^{+0.01}_{-0.01}$	$0.33^{+0.01}_{-0.01}$	$1.04^{+0.05}_{-0.05}$	$1.20^{+0.01}_{-0.01}$			Slab (-1)	3350/3384
	210^{+12}_{-14}	$1.05^{+0.01}_{-0.01}$	$0.64^{+0.04}_{-0.04}$	$0.79^{+0.04}_{-0.04}$	$2.85^{+0.02}_{-0.01}$			Cylinder (2)	3334/3384
	215^{+12}_{-13}	$1.01^{+0.01}_{-0.01}$	$0.60^{+0.04}_{-0.03}$	$0.86^{+0.05}_{-0.05}$	$1.73^{+0.01}_{-0.01}$			Cylinder (-2)	3336/3384
	227^{+10}_{-14}	$1.21^{+0.01}_{-0.02}$	$0.68^{+0.04}_{-0.03}$	$0.84^{+0.04}_{-0.04}$	$2.89^{+0.01}_{-0.02}$			Hemisphere (3)	3334/3384
	220^{+13}_{-11}	$1.14^{+0.01}_{-0.01}$	$0.66^{+0.03}_{-0.04}$	$0.90^{+0.05}_{-0.05}$	$1.71^{+0.02}_{-0.01}$			Hemisphere (-3)	3336/3384
	186^{+11}_{-9}	$0.66^{+0.01}_{-0.01}$	$0.45^{+0.02}_{-0.03}$	$0.77^{+0.04}_{-0.04}$	$0.866^{+0.004}_{-0.004}$			Sphere (4)	3341/3384
	191^{+13}_{-17}	$0.86^{+0.01}_{-0.01}$	$0.58^{+0.05}_{-0.04}$	$0.77^{+0.04}_{-0.04}$	$1.56^{+0.01}_{-0.01}$			Sphere (-4)	3337/3384
	196^{+13}_{-13}	$0.81^{+0.01}_{-0.01}$	$0.53^{+0.04}_{-0.04}$	$0.77^{+0.04}_{-0.04}$	$1.49^{+0.01}_{-0.01}$			Sphere (-5)	3337/3384

Table 4(b). Continuation of Table 4(a). Fit results with the thermal Comptonization model (for a sphere, the geometry parameter = 0) regarding the absorber, line component and the relative normalization, C_{ISGRI} , of a given X-ray spectrum with respect to ISGRI. See Section 4.1 for the definitions of the other parameters. The units of N_{H} , ξ and I_{Fe} are 10^{22} cm $^{-2}$, 10^{-2} erg cm s $^{-1}$, 10^{-4} cm $^{-2}$ s $^{-1}$, respectively, and ‘f’ denotes a fixed parameter.

State	X-ray spectrum	C_{ISGRI}	N_{H}^{f}	ξ	N_{H}^{p}	f^{p}	E_{Fe} (keV)	σ_{Fe} (keV)	I_{Fe}	w_{Fe} (eV)
Bright	EPIC pn (X1+X2)	$0.92^{+0.03}_{-0.03}$	$4.9^{+0.9}_{-0.7}$	10^{+79}_{-6}	$15.8^{+3.9}_{-3.3}$	$0.39^{+0.09}_{-0.07}$	$6.400^{+0.011}_{-0.011}$	$0.07^{+0.02}_{-0.01}$	$3.0^{+0.3}_{-0.3}$	83^{+7}_{-9}
	EPIC pn (X3)	$1.08^{+0.03}_{-0.03}$	$3.0^{+1.5}_{-1.8}$	64^{+47}_{-61}	$9.5^{+4.0}_{-1.1}$	$0.55^{+0.18}_{-0.22}$	$6.393^{+0.013}_{-0.012}$	$0.07^{+0.01}_{-0.01}$	$2.8^{+0.3}_{-0.3}$	76^{+9}_{-9}
	PCA PCU2 (B)	$1.17^{+0.03}_{-0.03}$	$7.4^{+0.4}_{-0.4}$	0f	0f	–	$6.06^{+0.08}_{-0.09}$	$0.36^{+0.15}_{-0.13}$	$6.8^{+1.3}_{-0.8}$	169^{+32}_{-20}
Medium	EPIC pn (X5)	$0.83^{+0.08}_{-0.06}$	$7.6^{+0.5}_{-0.4}$	4^{+11}_{-3}	$22.6^{+4.4}_{-1.5}$	$0.50^{+0.05}_{-0.04}$	$6.388^{+0.007}_{-0.007}$	$0.06^{+0.01}_{-0.01}$	$2.7^{+0.5}_{-0.3}$	149^{+27}_{-12}
	JEM-X (M)	$0.74^{+0.06}_{-0.06}$	$13.0^{+3.7}_{-3.3}$	0f	0f	–	–	–	–	–
Dim	EPIC pn (X4)	$1.17^{+0.01}_{-0.01}$	$6.36^{+0.14}_{-0.15}$	4^{+30}_{-3}	$23.5^{+0.6}_{-0.7}$	$0.69^{+0.01}_{-0.01}$	$6.398^{+0.004}_{-0.005}$	$0.06^{+0.01}_{-0.01}$	$2.3^{+0.1}_{-0.1}$	271^{+13}_{-13}
	XIS0,3 (D)	$1.11^{+0.01}_{-0.01}$	$8.03^{+0.12}_{-0.16}$	$0.7^{+0.9}_{-0.4}$	$28.8^{+0.9}_{-1.0}$	$0.50^{+0.01}_{-0.01}$	$6.384^{+0.003}_{-0.003}$	$0.03^{+0.01}_{-0.01}$	$2.2^{+0.1}_{-0.1}$	291^{+13}_{-13}
	XIS1 (D)	$1.13^{+0.01}_{-0.01}$		Fitted together with XIS0,3			$6.412^{+0.005}_{-0.004}$	$0.04^{+0.01}_{-0.01}$	$2.3^{+0.1}_{-0.1}$	280^{+13}_{-13}
	PCA PCU2 (D)	$1.16^{+0.01}_{-0.01}$	$13.6^{+0.5}_{-0.5}$	0f	0f	–	6.4f	0f	$2.1^{+0.3}_{-0.3}$	303^{+39}_{-39}

line (which are specific to a given X-ray detector within each of the states), respectively. The results in Table 4(b) and the entries for the bolometric model luminosity, $L_{X\gamma}$, in Table 4(a), are given only for the case of spherical geometry calculated using escape probability formalism (geometry 0).

We find the thermal Comptonization model to provide very good fits to the data. The values of the reduced χ^2 are $\lesssim 1$, which, however, appears not to be due to an overly complex model. In particular, the high-energy continua are determined only by three parameters, y , R , kT_e . For the bright state, Comptonization provides a much better fit than the e-folded power law, with $\Delta\chi^2$ of up to -14 . However, any trends seen for the geometry of the Comptonizing plasma are rather weak. In the case of the bright state, equally good models can be obtained with either a slab or a sphere. Also, models with seed photons being distributed within the source are of similar quality as those with localized seed photons. On the other hand, the differences between the models are slightly stronger in the case of the dim state. In particular, the slab model with seed photons at its bottom is somewhat better than that with the seed photons distributed throughout it. This can be a hint that the actual source has the seed photons external to the source rather than internal (which would be the case for the dominant synchrotron seed photons). We also note that the fitted values of kT_e are rather insensitive to the assumed geometry in both the bright and dim states. Our results for the bright state are similar to those of previous Comptonization fits, in particular to those of Z02, who obtained $kT_e = 73^{+34}_{-29}$ keV, $y = 0.88^{+0.12}_{-0.11}$ and $R = 0.60^{+0.24}_{-0.21}$ at $L_{X\gamma} \simeq 3.9 \times 10^{43}$ erg s $^{-1}$ using a broad-band X-ray spectrum from ASCA and OSSE.

In all geometries, we see in Table 4(a) that the Compton y parameter remains approximately constant between the bright and dim states, with only a slight decrease in the dim state. For the medium state, Table 4(a) gives the results only for the model with escape probabilities, for which the best-fitting y is almost the same as that in the dim state. These results are illustrated by the confidence contours shown in Fig. 5.

Apart from the results given in Tables 4(a) and (b), a reduction of χ^2 appears when the Fe abundance (assumed equal for the absorber and the reflector) is a free parameter. We found a moderate overabundance, 1.5 ± 0.2 times that of Anders & Ebihara (1982) for the bright state, with $\Delta\chi^2 = -6$, and 1.3 ± 0.1 for the dim state, $\Delta\chi^2 = -2$. For the *XMM-Newton* observation in 2000 December, an Fe overabundance of 2–3 was claimed by Schurch et al. (2003) but that fit was done with the *XMM-Newton* spectrum only and the reflection strength (affecting that determination) was not well constrained.

We also find that both the bright and dim state spectra prefer an inclination angle $>45^\circ$, with $\Delta\chi^2 = -3$ and -6 , respectively, at 75° . Since this effect is observed for symmetric (sphere) and asymmetric (hemisphere) geometries, we conclude that its main cause is the changing shape of the reflection component. On the other hand, allowing the reflector to be ionized does not improve the fit, and $\xi < 0.2$ erg cm s $^{-1}$ (at an assumed reflector temperature of 10^5 K).

The lack of the far-UV and very soft X-ray spectra does not allow us to fit the maximum temperature of the seed disc blackbody photons, kT_{bb} . We have found that changing it to either 5 or 20 eV yields no improvement of the fit. This is indeed expected given that the photon energies emitted by the disc are much below the fitted energy range, at which the shape of the Comptonization spectrum has already achieved a power-law shape independent of kT_{bb} .

Table 4(b) also shows the normalization of a given X-ray spectrum relative to that from ISGRI. For the bright state, when the

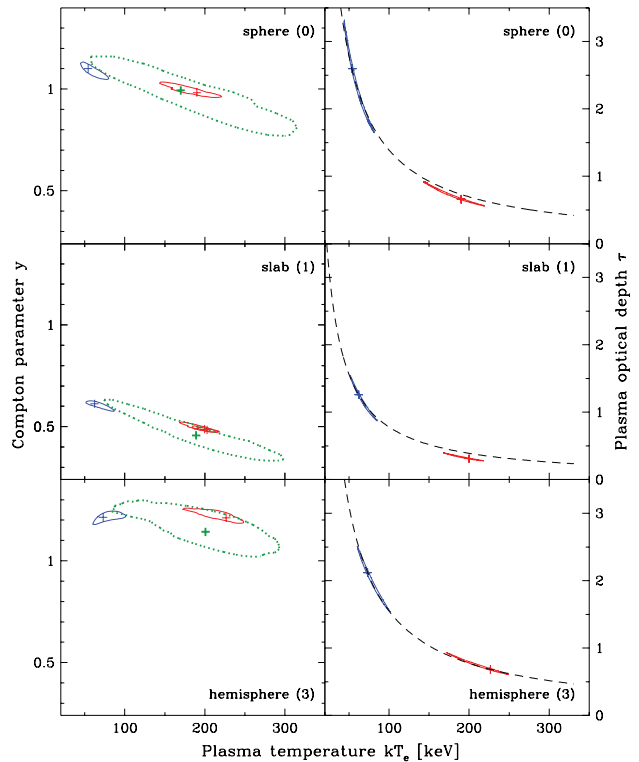


Figure 5. The 90 per cent confidence regions for the Compton y parameter (left) and the optical depth, τ (right), versus the temperature, kT_e for three geometries of the Comptonizing plasma. The solid blue, solid red and green dashed (only for y) contours correspond to the bright, dim and medium state, respectively. The dashed curves for τ versus kT_e correspond to $\tau \propto kT_e^{-1}$, normalized to the bright-state results.

INTEGRAL, *XMM-Newton* and *RXTE* observations were almost contemporary, C_{ISGRI} is very close to 1 and, for both of the *XMM-Newton* spectra, it follows the flux changes seen in the top panel of Fig. 3. This shows that ISGRI, EPIC pn and PCA detectors are well cross-calibrated. In the case of the two other spectral sets, the observations are not simultaneous. Nevertheless, C_{ISGRI} varies only within the range of 0.74–1.17, confirming the validity of our selection of the spectra for a given flux state.

We have also tested our results using the extended data sets (see Section 4.1). However, the quality of the fits and the plasma parameter uncertainty are not improved when they are used. This confirms that our selection of the primary sets was valid. Thus, we do not present here those results.

We note that even for such a bright AGN as NGC 4151, we have no data at energies $\gtrsim 200$ keV, as shown in Fig. 6. Still, for the dim state, we have found $kT_e \simeq 200$ keV with a statistical uncertainty of ~ 7 per cent or so. The physical reason for this low uncertainty is the observed lack of spectral curvature. In the process of thermal Comptonization, a power-law slope at $E \lesssim kT_e$ appears due to the merging of many individual up-scattering profiles, each being curved. The cut-off at $E \gtrsim kT_e$ is due to the electron energies being comparable to the photon ones, in which case a photon no longer increases its energy in a scattering. Since we see no cut-off up to ~ 200 keV, models with a lower kT_e are ruled out. On the other hand, models with a higher kT_e correspond to an increase of the photon energy in a single scattering by a factor of so large that the individual, curved, scattering profiles become clearly visible and the spectrum at $E \lesssim kT_e$ is no longer a power law. Since the

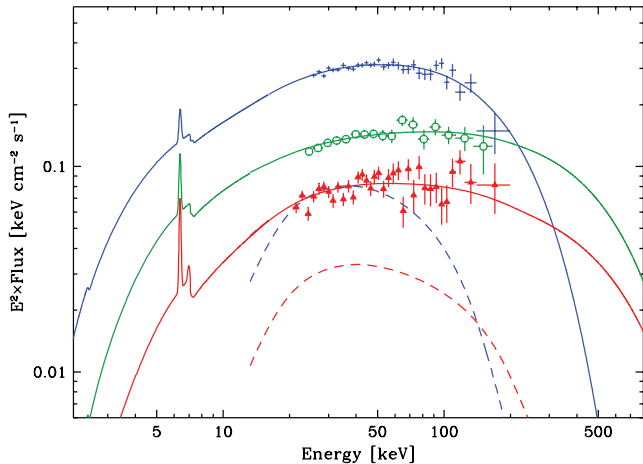


Figure 6. The Comptonization model spectra (solid curves; the geometry parameter = 0) of the three states of the NGC 4151, shown together with ISGRI spectra. The bright, medium and dim spectra are shown by the blue crosses, green circles and red triangles, respectively. The dashed curves show the reflection model components for the bright (upper) and dim states. The fitted JEM-X, *RXTE*, *XMM-Newton* and *Suzaku* spectra are not shown for clarity.

observed spectral shape is a power law, this case is also excluded. We note, however, that our assumed model corresponds to a single scattering zone. A power-law spectrum at $E \lesssim 200$ keV may also be produced by a superposition of emission regions with different temperatures (smoothing out the resulting spectrum), as e.g. in a hot accretion flow. In this case, the maximum temperature of the flow could be higher than 200 keV. In any case, we do see a very clear difference in the characteristic Comptonization temperature between the bright and dim state.

We comment here on the very high value of $kt_e = 315 \pm 15$ keV obtained by P01 for the 1999 January *BeppoSAX* spectrum of NGC 4151. The fit of that model appears rather poor when compared with the curvature of the *BeppoSAX*/PDS data above 50 keV (see fig. 2b in P01). We also find that the PDS spectrum is very similar to the average OSSE spectrum (Johnson et al. 1997), shown in Fig. 7 (with only the normalization of the PDS spectrum being about 5 per cent lower). This indicates that the source was in a moderately bright state in 1999 January, for which state the temperature of 315 keV appears highly unlikely. We cannot explain this discrepancy; it may be that $kt_e = 315 \pm 15$ keV represented a spurious local minimum.

As we see in Fig. 7, our bright-state model spectrum agrees well in shape with the average OSSE spectrum (Johnson et al. 1997). The latter also agrees with the first three points of the average NGC 4151 spectrum from *INTEGRAL*/SPI (Bouchet et al. 2008). However, the SPI 200–600 keV flux is implausibly high, which may reflect a problem with the background estimate. Indeed, the SPI analysis of Petry et al. (2009) yields only upper limits at $E > 150$ keV.

We see in Fig. 7 that the Comptonization models of the bright and dim states cross at ≈ 300 keV. Unfortunately, it is impossible to verify it with our data. In particular, we cannot test if there is any non-thermal component at high energy. Even the average spectrum from OSSE, the most sensitive detector up to date at $E \gtrsim 150$ keV, gives only a weak detection of NGC 4151 at $E \gtrsim 250$ keV with > 4 Ms exposure time. From the shown upper limits (including systematic errors) of the *INTEGRAL*/PICsIT, the most sensitive current detector at $E \gtrsim 250$ keV (Lubiński 2009), we see it would need > 10 Ms exposure time to detect NGC 4151 in the 300–400 keV range. Merging all the suitable *INTEGRAL* data (with the effective

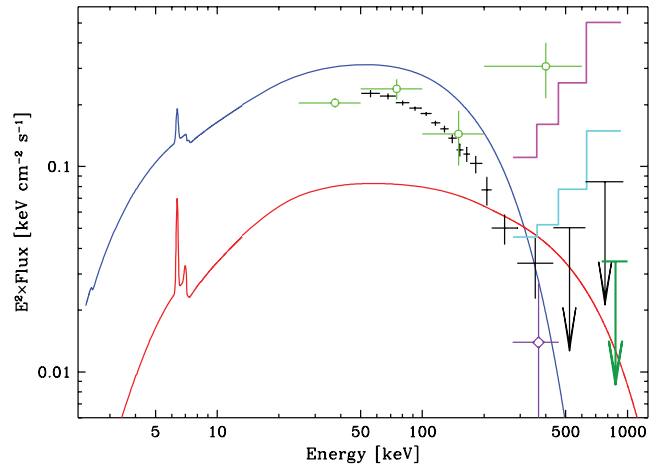


Figure 7. The Comptonization models for the extreme states (solid curves, same as in Fig. 6) compared to the average OSSE spectrum (crosses and two 2σ upper limits). The rightmost upper limit is the COMPTEL upper limit in the 0.75–1 MeV band (Maisack et al. 1995). The histograms give the *INTEGRAL*/PICsIT 3σ upper limits for 1 Ms (upper) and 10 Ms (lower) effective exposure time. The PICsIT 1.34 Ms average 277–461 keV flux is shown by error bars with a diamond. The SPI spectrum obtained by Bouchet et al. (2008) is shown by error bars with circles. Note that the 200–600 keV data point may be spurious.

exposure time of 1.34 Ms taken without the bright state, for which the observation was in the staring mode, not suitable for the PICsIT), we extracted the PICsIT flux in the 277–461 keV band. Although it is not a detection (and the shown error bar does not include systematic errors), it provides a hint that the average NGC 4151 emission in this energy range is weak.

5 DISCUSSION

5.1 Reflection and Fe line

5.1.1 Comparison with previous work

A reflection component in the X-ray spectra of NGC 4151 was first found by Zdziarski et al. (1996a), using contemporaneous data from *CGRO* and *Ginga*, yielding $R \simeq 0.43$ (using a Comptonization model and assuming $i = 65^\circ$). Then, Z02 found $R \simeq 0.6$ (at $i = 17^\circ$) using *CGRO* and *ASCA* data, and P01 found $R \simeq 0.2$ –1.8 using *BeppoSAX* data and a reflection model averaged over the viewing angle. A previous analysis of *INTEGRAL* bright-state data from 2003 May yielded a larger reflection, $R = 0.72 \pm 0.14$ (Beckmann et al. 2005), than that determined by us (their value of $kt_e = 94_{-10}^{+4}$ keV is also different from that found by us for the same data). By fitting the ISGRI and JEM-X bright-state spectra alone, we find results very similar to those with the *XMM-Newton* and *RXTE* spectra included (Tables 4a and b). Therefore, the differences appear to be a consequence of the substantial change of the *INTEGRAL* calibration since 2005. Furthermore, Beckmann et al. (2005) used the SPI spectra obtained in the staring observation mode, which can be affected by a large background uncertainty. Then, De Rosa et al. (2007) found $R \simeq 0.4$ for several *BeppoSAX* spectra and $R \simeq 0$ for the remaining ones, but using an e-folded power-law model rather than Comptonization. Then, Schurch & Warwick (2002) found $R \simeq 1.9$ using *XMM-Newton* data assuming $i = 65^\circ$, but this result was obtained using the 2.5–12 keV band only and assuming a fixed $\Gamma = 1.65$.

Regarding Fe K α line, Zdziarski et al. (1996a) found a narrow line with $I_{\text{Fe}} \simeq (0.6\text{--}1.0) \times 10^{-4} \text{ cm}^{-2} \text{ s}^{-1}$ using *Ginga* data, and Z02 found a narrow line at $I_{\text{Fe}} \simeq 2.5 \times 10^{-4} \text{ cm}^{-2} \text{ s}^{-1}$ accompanied by a weaker broad relativistic line using *ASCA* data. The broad component has not been observed later, whereas the narrow-line flux measured by *BeppoSAX* (De Rosa et al. 2007), *Chandra* (Ogle et al. 2000) and *XMM-Newton* (Schurch et al. 2003) was found to be in the range $(1.3\text{--}4.2) \times 10^{-4} \text{ cm}^{-2} \text{ s}^{-1}$. As seen in Tables 4(a) and (b), our results on R and I_{Fe} approximately agree with the previous measurements.

5.1.2 Close and distant reflector

We see in Table 4(a) that the relative strength of reflection, R , is close to being twice higher in the dim state than in the bright one. (In the medium state, the amount of data is very limited, and the apparent lack of detectable reflection may be not typical to that of flux level.) The increase of R with decreasing flux could be a real change of the solid angle subtended by the reflector between the states. On the other hand, it could be that it is due to the contribution of a distant reflector, in particular a molecular torus, as postulated in the AGN unified model. Reflection from distant media is indeed commonly seen in Seyferts 2 (see e.g. Reynolds et al. 1994). If we attribute the increase of R in the dim state due to that component, we can calculate the fractional reflection strength from the close reflector, presumably an accretion disc, and the flux reflected from the torus, which, due to its large size, is averaged over a long time-scale, and thus assumed to be the same in either state.

The hypothesis of the stable geometry of the source is supported by the approximate constancy of the Compton y parameter (see Table 4a and Fig. 5), and of the photon index, Γ (see Table 3). Those parameters are closely related to the amplification factor of Comptonization (e.g. Beloborodov 1999), whose constancy can be most readily achieved if the system geometry is constant (e.g. Haardt & Maraschi 1991; Zdziarski, Lubiński & Smith 1999). Thus, we consider an approximately constant relative reflection strength from the disc very likely. Observationally, we do see a strong R – Γ correlation in Seyferts and X-ray binaries, which can be interpreted by a geometrical feedback model (Zdziarski et al. 1999), and which would require a constant disc R for a given Γ .

The unabsorbed flux in a given state, F_S , where S = either D (dim) or B (bright), is the sum of the (unabsorbed) incident (i) and reflected (r) fluxes,

$$F_S = F_{i,S} + F_{r,S}, \quad (1)$$

where F_S and $F_{r,S}$ can be calculated from the results of our spectral fitting in Section 4.3. We assume that the observed (unabsorbed) reflected flux in each state is the sum of the close disc (d) state-dependent component and the constant distant torus (t) component,

$$F_{r,S} = F_{d,S} + F_t. \quad (2)$$

Then, assuming the constancy of the solid angle subtended by the disc reflector, or, equivalently, its reflection strength, R_d , the disc-reflected fluxes are

$$F_{d,S} = F_{r,S}(R_d/R_S), \quad (3)$$

where R_S is the reflection strength for a given state. We have four equations (2–3) for four unknowns, $F_{d,B}$, $F_{d,D}$, R_d and F_t , which can be readily solved. We note that they can be formulated without involving $F_{i,S}$, which implies that the solution does not depend on the choice of the energy interval in which the fluxes are measured

as long as it includes the entire reflected spectrum. The solutions for R_d and F_t are

$$R_d = \frac{(F_{r,B} - F_{r,D})R_B R_D}{F_{r,B}R_D - F_{r,D}R_B}, \quad F_t = \frac{(R_D - R_B)F_{r,B}F_{r,D}}{F_{r,B}R_D - F_{r,D}R_B}. \quad (4)$$

Then, the fractional reflection strength of the torus can be approximately estimated as

$$R_t \simeq \langle R \rangle (F_t / \langle F_r \rangle), \quad (5)$$

where $\langle R \rangle$ and $\langle F_r \rangle$ are the average observed reflection strength and the average reflected flux, respectively.

Using the values obtained for thermal Comptonization using escape probability formalism (geometry parameter = 0), we obtain $R_d = 0.27 \pm 0.07$, $F_t = (8.2 \pm 0.6) \times 10^{-11} \text{ erg cm}^{-2} \text{ s}^{-1}$ and $R_t = 0.24 \pm 0.04$ using either arithmetic or geometric averages in equation (5). Similar values are obtained for other Comptonization geometries considered in Section 4.3. We can check the robustness of our estimates by allowing the reflection strength to depend on the accretion rate, or flux. If we assume that R_d in the dim state is a half of that in the bright state [which requires an appropriate change of equation (3)], we obtain relatively similar values of the disc reflection in the bright state of $R_{d,B} = 0.23 \pm 0.12$, $F_t = (1.1 \pm 0.1) \times 10^{-10} \text{ erg cm}^{-2} \text{ s}^{-1}$ and $R_t = 0.32 \pm 0.04$.

Similar reasoning can be applied to the Fe K α line. The observed line photon flux in the state S, I_S , is assumed to be the sum of contributions from the disc, $I_{d,S}$ and the torus, I_t . The latter is assumed constant, and the former proportional to the ionizing flux incident on the disc. As a simplification, we assume the ionizing flux (≥ 7.1 keV for neutral Fe) to be proportional to the differential continuum photon flux, $F(E)/E$, at the line centroid energy, which we denote as N_S , and which is equal to I_S/w_S , where w_S is the observed equivalent width in a given state. This then implies a constant disc line equivalent width, w_d . Above, for the sake of simplicity, we have dropped the indices ‘Fe’, used in Section 4.3 and Table 4(b). The equations are

$$I_S = I_{d,S} + I_t, \quad I_{d,S} = w_d N_S, \quad (6)$$

which can be solved for

$$w_d = \frac{I_B - I_D}{N_B - N_D}, \quad I_t = \frac{I_D N_B - I_B N_D}{N_B - N_D}. \quad (7)$$

The equivalent width of the torus line flux with respect to the average incident photon flux, $\langle N \rangle$, can be estimated as

$$w_t = I_t / \langle N \rangle. \quad (8)$$

For the numerical values, we use here averages of the fit results both for EPIC pn spectra in the bright state and for the EPIC pn and XIS spectra in the dim state (see Table 4b). We find $I_B = (2.9 \pm 0.2) \times 10^{-4} \text{ cm}^{-2} \text{ s}^{-1}$, $I_D = (2.3 \pm 0.1) \times 10^{-4} \text{ cm}^{-2} \text{ s}^{-1}$, $N_B = (3.6 \pm 0.1) \times 10^{-3} \text{ keV}^{-1} \text{ cm}^{-2} \text{ s}^{-1}$ and $N_D = (8.1 \pm 0.1) \times 10^{-4} \text{ keV}^{-1} \text{ cm}^{-2} \text{ s}^{-1}$. This yields $w_d = 23 \pm 11 \text{ eV}$, $I_t = (2.1 \pm 0.9) \times 10^{-4} \text{ cm}^{-2} \text{ s}^{-1}$ and $w_t = 93 \pm 41 \text{ eV}$, $120 \pm 53 \text{ eV}$ using the arithmetic or geometric average, respectively.

The equivalent width of the Fe line at $i = 45^\circ$ by an isotropically illuminated cold disc for $\Gamma = 1.75$ is $\simeq 140 \text{ eV}$ (George & Fabian 1991). The value of $R_d \simeq 0.27$ found based on the observed reflection strength then implies $w_d \sim 38 \text{ eV}$, somewhat higher than the estimate based on the line fluxes, but still in an approximate agreement taking into account measurement errors and a number of assumptions we have made. On the other hand, $R_t \simeq 0.24$ found above would explain only $w_t \sim 30 \text{ eV}$. However, we note that we have neglected the local absorber, which obviously also gives rise

to an Fe $K\alpha$ line component. Its characteristic N_{H} of $\sim 10^{23} \text{ cm}^{-2}$ (Table 4b) can readily explain the excess equivalent width of $\sim 70 \text{ eV}$ (e.g. Makishima 1986; Awaki et al. 1991) of the constant line component with respect to that expected from the torus.

We note a number of caveats for our results. The standard accretion disc is flared, not flat (Shakura & Sunyaev 1973). This, however, would have a relatively minor effect, changing somehow the distribution of the inclination angles. Our results indicate disc reflection with R_{d} substantially less than unity, which implies the $X\gamma$ source is not entirely above the disc. A likely geometry explaining it is a hot inner flow surrounded by a disc (e.g. Abramowicz et al. 1995; Narayan & Yi 1995; Yuan 2001), in which case the incident radiation will have much larger incident angles (measured with respect to the axis of symmetry) than those assumed in the used model (Magdziarz & Zdziarski 1995). The disc may be warped (e.g. Wijers & Pringle 1999), which again would change the distribution of the incident angles. Furthermore, Compton scattering in the hot plasma above the disc reduces the observed reflection strength (Petrucci et al. 2001b).

Then, we also used the slab geometry for the torus reflection. Thus, the obtained solid angle does not correspond to the actual angle subtended by the torus from the X-ray source. For example, Murphy & Yaqoob (2009) considered a torus with a circular cross-section subtending (as seen from the centre) a 2π solid angle. They found that the reflection component in this case is several times weaker than that corresponding to a slab subtending the same angle. One obvious effect here is that, unlike the case of a slab, an observer sees only a fraction of the reflecting surface, without parts obscured by the torus itself. If we take this into account, our value of $R_{\text{t}} \sim 0.2$ appears consistent with a torus subtending a $\sim 2\pi$ solid angle. We note, however, that even if the torus solid angle is formally 2π or so, a large part of it will be shielded from the X-ray source by the accretion disc and the black hole itself, so the actual irradiated solid angle may be substantially lower. This effect was not taken into account in the geometrical model of Murphy & Yaqoob (2009). Furthermore, the cross-section of the torus may be substantially different from circular, which may increase the observed reflection, as well as it may be clumpy (Krolik & Begelman 1988; Nenkova, Ivezić & Elitzur 2002), which will decrease it. Still, our value of $w_{\text{t}} \sim 100 \text{ eV}$ agrees with that from a torus with the column density of $N_{\text{H}} \sim 10^{24} \text{ cm}^{-2}$ for $\Gamma \simeq 1.75$ (Murphy & Yaqoob 2009), which provides an explanation for that equivalent width alternative, or additional, to that as being due to the line emission of the absorber (discussed above).

We have assumed that the torus reflection component is constant on the time-scale of years. On the other hand, Minezaki et al. (2004) found that the dusty torus inner boundary is at $\simeq 0.04 \text{ pc}$. Thus, a fraction of the torus reflection may vary on the corresponding time-scale of $\sim 50 \text{ d}$. Furthermore, 0.04 pc corresponds to $\simeq 2 \times 10^4 R_{\text{g}}$ (where $R_{\text{g}} \equiv GM/c^2$ is the gravitational radius), where the accretion disc may still be present and join on to the torus. On the other hand, Radomski et al. (2003) have constrained the torus outer boundary to $\lesssim 35 \text{ pc}$, so the bulk of the torus reflection may still be constant over a time-scale of years.

5.2 Absorber properties

We compare our results with those based on *BeppoSAX*, which also provided broad-band spectra, allowing to simultaneously determine absorber properties and the continuum. They were studied by Puccetti et al. (2007) and De Rosa et al. (2007), who used

the same absorber model as in this work. We find their results to be compatible with ours. The fully covering absorber has $N_{\text{H}} \simeq (0.9\text{--}9.4) \times 10^{22} \text{ cm}^{-2}$ for *BeppoSAX* and $\simeq (3.0\text{--}8.1) \times 10^{22} \text{ cm}^{-2}$ in our case (see Table 4b). For the partially covering absorber, $N_{\text{H}}^{\text{p}} \simeq (3.5\text{--}30.3) \times 10^{22} \text{ cm}^{-2}$ (*BeppoSAX*) and $\simeq (9.5\text{--}30.2) \times 10^{22} \text{ cm}^{-2}$ (this work). The covering fractions are also similar, $f^{\text{p}} \simeq 0.34\text{--}0.71$ (*BeppoSAX*) and $0.36\text{--}0.71$ (this work). The only exception is the long-exposure *BeppoSAX* observation of NGC 4151 in 2001 December showing a very low N_{H} (De Rosa et al. 2007).

We find an anticorrelation between the N_{H} of both absorber components and the hard X-ray flux. We define the total column, $N_{\text{H}} = N_{\text{H}}^{\text{i}} + f^{\text{p}} N_{\text{H}}^{\text{p}}$. For the bright state, we have $N_{\text{H}}/10^{22} \text{ cm}^{-2} = 11.1 \pm 3.5$ (*XMM-Newton* X1+X2) and 8.2 ± 4.9 (X3), for the medium state, 18.0 ± 2.8 (*XMM-Newton* X5), and for the dim state, 23.1 ± 0.8 (*XMM-Newton* X4) and 23.2 ± 0.9 (*Suzaku*). Also, the covering fraction is anti-correlated with the hard X-ray flux (see Table 4b). A similar trend is seen for the results of Puccetti et al. (2007), who used the 6–10 keV for the X-ray flux. The variable part of the absorber needs to be relatively close to the X-ray source to be able to follow its flux on the time-scale of days. The absorber in NGC 4151 was identified with massive outflows from the accretion disc (Piro et al. 2005), a broad-line region (Puccetti et al. 2007) or the surface or wind of the torus (Schurch & Warwick 2002). Only the disc wind is close enough to the X-ray source to follow the change of the nuclear emission and to produce any correlation. The physical explanation for the correlation remains unclear; possibly the wind rate in NGC 4151 decreases with increasing accretion rate.

5.3 The nature of the X-ray source

The geometry and parameters of the source are constrained by a number of our findings. We find (i) that both the Compton parameter and the X-ray spectral index are approximately the same in both bright and dim states (Sections 4.2–4.3). This implies an approximately constant amplification ratio of the Comptonization process, i.e. the ratio of the power emitted by the plasma to that supplied to it by seed photons (e.g. Beloborodov 1999). The amplification factors obtained with the Comptonization model are indeed similar, $A = 17 \pm 2$, 15 ± 2 for the bright and dim states, respectively (assuming $kT_{\text{bb}} = 10 \text{ eV}$). A similar value of $A \simeq 13$ was obtained for a Comptonization model fitted to the 1991 data from *ROSAT*, *Ginga* and *OSSE* (Zdziarski et al. 1996a).

If the seed photons are supplied by an accretion disc surrounding the hot plasma, this implies an approximately constant disc inner radius. Based on this, we have inferred (ii) a relatively weak reflection from the disc, $R_{\text{d}} \simeq 0.3$ (Section 5.1.2). This qualitatively agrees with $A \gg 1$ and both findings rule out the static disc corona geometry; the (outer) disc subtends a small solid angle as seen from the X-ray source, and the X-ray source subtends a small solid angle as seen from inner parts of the disc (Zdziarski et al. 1999). An implication of the latter is that the modelled disc black-body emission (which provides seed photons for Comptonization) should be much weaker than that observed (which corresponds to the entire disc emission). This seems to be indeed the case as shown in Fig. 8, where we see that the bright-state UV flux inferred from the Comptonization model is about an order of magnitude below the shown maximum observed far-UV (1350 Å; 9.2 eV) flux. On the other hand, the model dim-state far-UV flux is close to the historical minimum observed. However, that minimum represented a single isolated dip in the light curve (Kraemer et al. 2006), and the actual far-UV flux corresponding to the dim state is likely to be significantly higher. In choosing the shown range of the far-UV flux

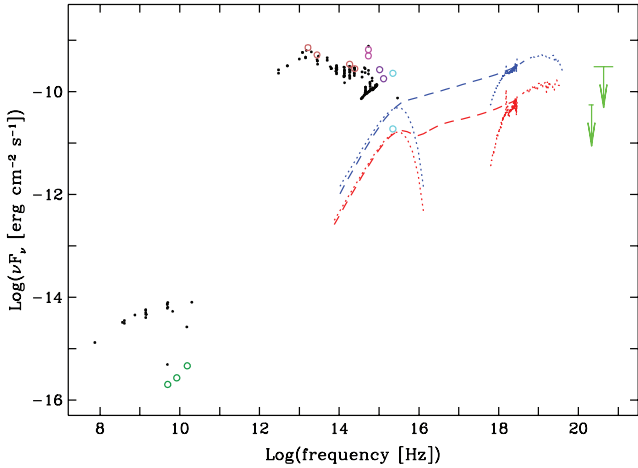


Figure 8. The broad-band spectrum of NGC 4151. The radio, IR, optical and UV data (black dots) were taken from the NED data base. Additional data are shown in circles in radio (green; Ulvestad et al. 2005), mid and near IR (brown, Radomski et al. 2003; Ruiz et al. 2003), optical (magenta, OMC, this work) and UV (purple, *Swift*/UVOT, this work; and cyan, *HST*/STIS, the flux extrema from fig. 3 of Kraemer et al. 2006). The *XMM-Newton* EPIC pn and ISGRI spectra of the bright and dim states are shown by the blue and red dots, respectively; the corresponding unabsorbed Comptonization models below 10 keV are shown by dashes, and the disc blackbody (assuming geometry parameter = 0 and $kT_{\text{bb}} = 5$ eV) incident on the hot plasma are shown by the dotted curves. The upper limits in the 0.75–1–3 MeV energy ranges are from COMPTEL (Maisack et al. 1995).

we used its strong correlation with the optical flux, which can be seen by comparing Fig. 1(d) with fig. 1 in Kraemer et al. (2006).

The IR, optical and UV fluxes shown in Fig. 8 appear relatively weakly affected by the host galaxy emission. In particular, the dominance of the AGN in the *U* band is shown by its strong variability (Czerny et al. 2003). In the optical range, there can be some non-negligible fraction of emission from the broad- and narrow-line regions, but in the UV we expect that the disc dominates. Given that the measured UV emission is, furthermore, absorbed by the host galaxy, the conclusion above that only a small fraction of the disc emission undergoes Comptonization appears secure.

Another result is (iii) the connection of the normalization of the fitted disc blackbody seed emission to the disc inner radius, R_{in} . Based on the definition from XSPEC, we can express it as

$$K = \frac{10^8 r \cos i (R_{\text{in}}/10^{12} \text{ cm})^2}{f_{\text{col}}^4 (D/10 \text{ Mpc})^2}, \quad (9)$$

where $f_{\text{col}} \sim 1.7$ is the colour correction to the blackbody temperature (Shimura & Takahara 1995), and r is the ratio of the blackbody emission incident on the plasma to that emitted by the disc. It implies (at $D = 13.2$ Mpc and $i = 45^\circ$)

$$R_{\text{in}} \simeq 4.5 \times 10^{13} \left(\frac{K}{10^9}\right)^{1/2} \left(\frac{r}{0.1}\right)^{-1/2} \left(\frac{f_{\text{col}}}{1.7}\right)^2 \text{ cm}. \quad (10)$$

At $M = 4.6 \times 10^7 M_\odot$ (Bentz et al. 2006), $R_g \simeq 6.8 \times 10^{12}$ cm. Thus, the values of K in Table 4(a) for the bright state (at $T_{\text{bb}} = 10$ eV) imply $R_{\text{in}} \sim 6R_g$, the last stable orbit for a non-rotating black hole. This is in conflict with the findings above, according to which the inner part of the flow is occupied by the hot plasma and not by the disc, unless the black hole is rotating fast. Furthermore, the DISKBB model used for the seed photons becomes invalid when R_{in} is close to the last stable orbit with the standard zero-stress boundary condition (Gierliński et al. 1999). We note, however, the

disc flux is $\propto R_{\text{in}}^2 T_{\text{bb}}^4$, and approximately $R_{\text{in}} \propto T_{\text{bb}}^{-2}$ for a given X-ray spectrum. In particular, $K = 7.2 \times 10^9$ for the bright state at $kT_{\text{bb}} = 5$ eV (consistent with the UV data) and the geometry parameter = 0, confirming the above scaling. This yields $R_{\text{in}} \simeq 18R_g$, allowing the existence of a hot inner flow. Given that agreement, we used $kT_{\text{bb}} = 5$ eV in the models shown in Fig. 8. We note that if $R_{\text{in}} \simeq$ constant, kT_{bb} has to be somewhat lower in the dim state.

For comparison, the radius, R_{eq} , at which the integrated gravitational energy dissipation at $R > R_{\text{eq}}$ equals that at $R < R_{\text{eq}}$ is $R_{\text{eq}} \simeq 14.7R_g$ for a non-rotating black hole in the pseudo-Newtonian approximation (Paczynski & Wiita 1980) and with the zero-stress boundary condition at the last stable orbit, and less for a rotating black hole. Thus, $R_{\text{in}} \sim R_{\text{eq}}$, as found above, is consistent with the observed energy distribution of NGC 4151, showing the optical/UV emission (presumably due to the disc) at a similar level as that at ~ 100 keV (due to the hot flow). Note that R_{in} moderately larger than R_{eq} is required if some fraction of the energy dissipated below R_{in} is advected to the black hole instead of being radiated away. However, a disc truncated at $R_{\text{in}} \gg R_{\text{eq}}$ would be in strong conflict with the broad-band spectrum, as it implies the disc UV emission much weaker than that of X-rays. A prediction of this result is a presence of an Fe $K\alpha$ line only moderately relativistically broadened (as found earlier by Z02).

The reflection of $R_d \simeq 0.3$ may be easily achieved if the central hot region (with a large scale height) is surrounded by a disc. We have calculated the reflection strength in some simple geometrical models, with a sphere and cylinder surrounded by a flat disc. For the sphere and cylinder with the height equal to 1/2 of its radius we find $R_d \simeq 0.29$ and 0.26, respectively, in agreement with our estimate. At this R_d , the emission of the parts of the disc close to the hot flow is most likely dominated by reprocessing of X-rays, in agreement with the constancy of the y parameter (Zdziarski et al. 1999). As a caveat, we point out that the geometrical R_d estimates are highly simplified, not taking into account the actual hot flow geometry and the radial distribution of the Comptonized emission. We also note that the constancy of the y parameter can also be explained in a model in which the inner disc radius increases in the dim state, but at the same time the energy dissipation in the hot flow becomes relatively stronger in its outer region, e.g. due to advection.

On the other hand, the effective solid angle subtended by the hot flow as seen from the disc can be identified with our parameter $r \sim 0.1$ above. All the above considerations very strongly argue for the Comptonizing plasma in NGC 4151 being photon starved. This is not compatible with a static corona above the disc (Haardt & Maraschi 1991), and compatible with a hot inner flow surrounded by an outer cold disc. However, it is also possible that the corona does cover the disc but it is in a state of a mildly relativistic outflow (Beloborodov 1999; Malzac, Beloborodov & Poutanen 2001). The relativistic motion then both reduces the flux of the up-scattered photons incident on the disc, which explains the relative weakness of the disc reflection, and reduces the flux of the disc blackbody photons entering the corona in its comoving frame, which explains the photon starvation of the hot plasma, i.e. $A \gg 1$. A prediction of this model is the presence of a very broad relativistic Fe line (as the disc now extends all the way to the minimum stable orbit). The lack of detection of such a line in high-quality *XMM-Newton* and *Suzaku* spectra represents an argument against this model.

Our next finding has been that (iv) the plasma temperature increased by a factor of $\simeq 3.5$ when the bolometric X-ray luminosity decreased by about the same factor (see Table 4a). In agreement with the approximate constancy of y , the optical depth also decreased by a similar factor. This can be explained if the accretion

rate, \dot{M} , is $\propto L_{X\gamma}$ and the hot flow has a velocity profile independent of \dot{M} , so $\tau \propto L_{X\gamma}$. The temperature then follows from the energy balance provided the ratio of the power in the hot flow emission to that in seed photons cooling remains constant. However, models of accreting hot flows yield a dependence of τ on $L_{X\gamma}$ weaker than the simple proportionality [e.g. equations (10–11) in Zdziarski 1998; table 2 in Yuan & Zdziarski 2004].

The total model luminosity of the Comptonization component (including reflection) in the bright and dim state is $L_{X\gamma} \simeq 5.2 \times 10^{43} \text{ erg s}^{-1}$ and $1.5 \times 10^{43} \text{ erg s}^{-1}$, respectively (see Table 4a). The estimated average luminosity from the IR to UV is $\simeq 7 \times 10^{43} \text{ erg s}^{-1}$, with the IR band ($< 10^{14} \text{ Hz}$) contributing ~ 60 per cent of it. If we then assume that the IR flux remains constant and the optical–UV flux scales as the high-energy emission, the total bolometric luminosity can be estimated as $1.3 \times 10^{44} \text{ erg s}^{-1}$, $7 \times 10^{43} \text{ erg s}^{-1}$ in the bright and dim states, respectively. Assuming the hydrogen mass fraction of $X = 0.7$ and $M = 4.6 \times 10^7 M_{\odot}$, the Eddington luminosity $L_E \equiv 8\pi G M m_p c / [(1 + X)\sigma_T] \simeq 6.8 \times 10^{45} \text{ erg s}^{-1}$, giving the Eddington ratios of $\simeq 0.01$ – 0.02 . Note the factor of 2 variability of the bolometric luminosity compared to the factor of 3.5 variability of the Comptonization component. This difference appears to be explained by the presence of the constant, averaged over very long time-scales, IR component.

Relevant time-scales include the light crossing time across the circumference of the last stable orbit, which for a non-rotating black hole is $\sim 2700 \text{ s}$ (at the default mass). The corresponding light crossing time at $R_{\text{in}} \sim 15 R_g$ is $\sim 7000 \text{ s}$. Thus, the hour-time-scale variability observed by ISGRI in the bright state (Fig. 3) appears to correspond to fluctuations at those radii. On the other hand, the viscous time of an accretion flow is

$$t_{\text{visc}} = \frac{GM}{c^3} \left(\frac{R}{R_g} \right)^{3/2} \alpha^{-1} \left(\frac{H}{R} \right)^{-2} \simeq 1.2 \times 10^6 \text{ s} \left(\frac{R}{15 R_g} \right)^{3/2} \times \left(\frac{M}{4.6 \times 10^7 M_{\odot}} \right) \left(\frac{\alpha}{0.1} \right)^{-1} \left(\frac{H/R}{1/3} \right)^{-2}, \quad (11)$$

where H is the flow scaleheight, α is the viscosity parameter and $H/R \sim 1/3$ for a hot flow. At our default mass, $15 R_g$ and $\alpha = 0.1$, $t_{\text{visc}} \simeq 13 \text{ d}$. For comparison, the *Swift*/BAT data for NGC 4151 need to be rebinned to several days in order to get a sufficient signal-to-noise ratio for low flux states. Thus, this detector can sample the overall behaviour of the hot flow but not variability close to the last stable orbit.

The spectrum of NGC 4151 resembles spectra of black hole binaries in the hard state, also commonly fitted by thermal Comptonization. However, a faint non-thermal tail has occasionally been seen there (see e.g. McConnell et al. 2002; Wardziński et al. 2002). The Comptonization model used by us also allows to include a corresponding non-thermal tail to the electron distribution. However, the data for NGC 4151 do not allow us to test for the presence of any non-thermal spectral component (see Section 4.3).

5.4 Comparison with other objects

We have presented the average parameters of Seyfert spectra in Section 1, for both e-folded power law and Comptonization models. Our results for NGC 4151 are within the range observed for other Seyferts, as noted by Z02. Z02 also provide a critical analysis of earlier finding of very hard X-ray spectra in NGC 4151, which they find to result from improper modelling of its complex absorption. NGC 4151 in the bright state is only slightly harder than the average Seyfert 1, and it shows less reflection, in accordance with

the reflection-index correlation (Zdziarski et al. 1999). On the other hand, the dim state appears to have a significant contribution to reflection from a distant reflector, possibly a torus (Section 5.1.2).

The similarity between spectra of Seyferts and black hole binaries in the hard spectral state was pointed out by, e.g. Zdziarski et al. (1996b), though the latter appear to have on average somewhat harder spectra. This is likely to be due to the disc seed photon energies being much higher than those in Seyferts, which reduces the spectral index, Γ , for a given Comptonization amplification factor, A (Beloborodov 1999).

A striking similarity between the OSSE spectra of the black hole binary GX 339–4 in the hard state and NGC 4151 was pointed out by Zdziarski et al. (1998). Wardziński et al. (2002) have shown that when $L_{X\gamma}$ of GX 339–4 decreased by a factor of ~ 2 , kT_e increased significantly (see their fig. 1a), from 46_{-4}^{+6} keV to 76_{-6}^{+5} keV , with only a slight softening of the X-ray slope. This effect is very similar to that seen in NGC 4151 (see Table 4a). In both NGC 4151 and GX 339–4, this effect may be due to a decrease of \dot{M} in the hot flow causing the associated reduction of τ .

6 CONCLUSIONS

We have presented a comprehensive spectral analysis of all *INTEGRAL* data obtained so far for NGC 4151, together with all contemporaneous data from *RXTE*, *XMM–Newton*, *Swift* and *Suzaku* (Section 2). Our main findings are summarized below.

We have found that the 20–100 keV emission measured by *INTEGRAL* has had almost the same range of fluxes as that measured by other satellites during past 40 yr (Section 3). Thus, our analysis appears to explore the full range of the variability of this object. Also, we have found that this flux appears to uniquely determine the intrinsic broad-band spectrum.

Simultaneous observations by *INTEGRAL* in the optical range and in medium and hard X-rays show a very strong correlation within the X-ray band, and a less clear correlation between the optical and X-ray emission, with a bimodal behaviour of the optical flux. The linearity of the former correlation shows that the X-ray spectral slope of NGC 4151 remains almost constant.

Most of the *INTEGRAL* observations correspond to either a bright or dim hard X-ray state (Section 4.1). We have found that a thermal Comptonization model provides very good fits to the data (Section 4.3). As the state changes from bright to dim (with $L_{X\gamma}$ decreasing by a factor of $\simeq 3.5$), the plasma electron temperature increases from $kT_e \sim 60$ to $\sim 200 \text{ keV}$ and the Thomson optical depth decreases from $\tau \sim 2$ to ~ 0.6 (for spherical geometry), i.e. $\tau \propto 1/kT_e$ and $\tau \propto L_{X\gamma}$. The former proportionality corresponds to an almost constant Compton y parameter, with the X-ray slope remaining almost constant, with only a slight softening in the dim state, in agreement with the medium/hard X-ray correlation. This is suggestive of almost constant source geometry and amplification factor. The latter proportionality may occur due to the accretion rate varying at an approximately constant hot flow velocity.

The fitted strength of Compton reflection increased from $R \simeq 0.4$ to $R \simeq 0.8$, which, at the face value, would be in conflict with the constant source geometry indicated by the constant y . However, in accordance with the AGN unified model, NGC 4151 is likely to possess a remote torus, also reflecting the central X-ray emission. Assuming the solid angles subtended by both the (close) disc reflector and the (distant) torus reflector are constant, we can explain the varying fitted reflection strength by the presence of a contribution of the flux reflected by the torus, which is constant over the observation time-scale given its very large size (Section 5.1.2).

In the bright state, the contribution of the torus reflection is small, but it becomes much stronger in the dim state, explaining the fitted large value of R . Given the above assumption, we find that the solid angles subtended by the disc and torus (as seen from the X-ray source) are $\simeq 0.3$, 0.2 of 2π , respectively. These values have been obtained with a slab reflection model, which is likely to substantially underestimate the actual solid angle subtended by the torus, which might then be close to 2π .

The Comptonizing plasma is photon-starved, i.e. the flux in seed photons incident on the plasma is ~ 15 times weaker than the Comptonized flux (Section 5.3). This is consistent with the seed photons being supplied by a truncated optically thick disc surrounding a hot accretion flow. This geometry is also consistent with the relatively small disc reflection. We also find that the flux of the disc photons fitted to the X-ray spectra is an order of magnitude below the UV fluxes actually observed. This is again consistent with the above geometry, in which only a small fraction of the emitted disc photons is incident on the inner hot regions. All these findings rule out a static disc corona geometry. However, they are still compatible with a corona outflowing at a mildly relativistic speed (see Section 5.3).

In any case, the disc inner radius cannot be very large given that the observed EF_E at UV are of the same order as those at hard X-rays, implying a rough equipartition between the disc and hot flow emission. For a non-rotating black hole, the radius with the same integrated dissipation below and above it is $\simeq 15R_g$. The truncation radius can also be constrained by the fitted Comptonization model, which assumes the seed photons are disc blackbody. This gives a similar value of R_{in} for the inner disc temperature of ~ 5 eV, which is consistent with the observations.

Compared to Seyfert 1s, NGC 4151 has a somewhat harder X-ray spectrum and less reflection. Its spectrum is also similar to black hole binaries in the hard state, in particular to GX 339–4, which has shown a very similar spectral evolution.

Future missions, e.g. *Astro-H* and *EXIST*, with instruments with a sensitivity comparable to that of OSSE, can provide better data above 200 keV than obtained up to date. Yet, for a better understanding of the physics of the central engine of AGNs, we need high-quality data up to at least 1 MeV. This would yield strong constraints on the electron distribution in the Comptonization region (e.g. the presence of a non-thermal tail) and on the source geometry (e.g. the spatial distribution of the electron temperature and the characteristic optical depth).

ACKNOWLEDGMENTS

We thank B. Czerny for valuable discussions. PL and AAZ have been supported in part by the Polish MNiSW grants NN203065933 and 362/1/N-INTEGRAL/2008/09/0. We used data from the High Energy Astrophysics Science Archive Research Center, and from the NASA/IPAC Extragalactic Data base.

REFERENCES

- Abramowicz M. A., Chen X., Kato S., Lasota J.-P., Regev O., 1995, *ApJ*, 438, L37
- Anders E., Ebihara M., 1982, *Geochim. Cosmochim. Acta*, 46, 2363
- Arnaud K. A., 1996, in Jacoby G. H., Barnes J., eds, *ASP Conf. Ser. Vol. 101, Astronomical Data Analysis Software and Systems V*, Astron. Soc. Pac., San Francisco, p. 17
- Awaki H., Koyama K., Inoue H., Halpern J. P., 1991, *PASJ*, 43, 195
- Bałucińska-Church M., McCammon D., 1992, *ApJ*, 400, 699
- Beckmann V., Shrader C. R., Gehrels N., Soldi S., Lubiński P., Zdziarski A. A., Petrucci P.-O., Malzac J., 2005, *ApJ*, 634, 939
- Beckmann V. et al., 2009, *A&A*, 505, 417
- Beloborodov A. M., 1999, *ApJ*, 510, L123
- Bentz M. C. et al., 2006, *ApJ*, 651, 775
- Bouchet L., Jourdain E., Roques J.-P., Strong A., Diehl R., Lebrun F., Terrier R., 2008, *ApJ*, 679, 1315
- Courvoisier T. J.-L. et al., 2003, *A&A*, 411, L53
- Czerny B., Niñołajuk M., Piasecki M., Kuraszewicz J., 2001, *MNRAS*, 325, 865
- Czerny B., Doroshenko V. T., Niñołajuk M., Schwarzenberg-Czerny A., Loska Z., Madejski G., 2003, *MNRAS*, 342, 1222
- Dadina M., 2008, *A&A*, 485, 417
- Das V. et al., 2005, *AJ*, 130, 945
- De Rosa A., Piro L., Perola G. C., Capalbi M., Cappi M., Grandi P., Maraschi L., Petrucci P. O., 2007, *A&A*, 463, 903
- Done C., Mulchaey J. S., Mushotzky R. F., Arnaud K. A., 1992, *ApJ*, 395, 275
- Finoguenov A. et al., 1995, *A&A*, 300, 101
- George I. M., Fabian A. C., 1991, *MNRAS*, 249, 352
- Gierliński M., Zdziarski A. A., Poutanen J., Coppi P. S., Ebisawa K., Johnson W. N., 1999, *MNRAS*, 309, 496
- Haardt F., Maraschi L., 1991, *ApJ*, 380, L51
- Johnson H. L., 1966, *ARA&A*, 4, 193
- Johnson W. N., McNaron-Brown K., Kurfess J. D., Zdziarski A. A., Magdziarz P., Gehrels N., 1997, *ApJ*, 482, 173
- Kraemer S. B. et al., 2006, *ApJS*, 167, 161
- Krolik J. H., Begelman M. C., 1988, *ApJ*, 329, 702
- Lubiński P., 2009, *A&A*, 496, 557
- Magdziarz P., Zdziarski A. A., 1995, *MNRAS*, 273, 837
- Magdziarz P., Blaes O. M., Zdziarski A. A., Johnson W. N., Smith D. A., 1998, *MNRAS*, 301, 179
- Maisack M. et al., 1995, *A&A*, 298, 400
- Makishima K., 1986, in Mason K. O., Watson M. G., White N. E., eds, *The Physics of Accretion on to Compact Objects*. Springer, Berlin, p. 249
- Malzac J., Beloborodov A. M., Poutanen J., 2001, *MNRAS*, 326, 417
- McConnell M. L. et al., 2002, *ApJ*, 572, 984
- Minezaki T., Yoshii Y., Kobayashi Y., Enya K., Suganuma M., Tomita H., Aoki T., Peterson B. A., 2004, *ApJ*, 600, L35
- Mitsuda K. et al., 1984, *PASJ*, 36, 741
- Murphy K. D., Yaqoob T., 2009, *MNRAS*, 397, 1549
- Narayan R., Yi I., 1995, *ApJ*, 452, 710
- Neškova M., Ivezić Ž., Elitzur M., 2002, *ApJ*, 570, L9
- Ogle P. M., Marshall H. L., Lee J. C., Canizares C. R., 2000, *ApJ*, 545, L81
- Paczyński B., Wiita P. J., 1980, *A&A*, 88, 23
- Parsons A. M., Gehrels N., Paciesas W. S., Harmon B. A., Fishman G. J., Wilson C. A., Zhang S. N., 1998, *ApJ*, 501, 608
- Perotti F. et al., 1991, *ApJ*, 373, 75
- Petrucci P. O. et al., 2000, *ApJ*, 540, 131
- Petrucci P. O. et al., 2001a, *ApJ*, 556, 716 (P01)
- Petrucci P. O., Merloni A., Fabian A., Haardt F., Gallo E., 2001b, *MNRAS*, 328, 501
- Petry D., Beckmann V., Halloin H., Strong A., 2009, *A&A*, 507, 549
- Piro L., De Rosa A., Matt G., Perola G. C., 2005, *A&A*, 441, L13
- Poutanen J., Svensson R., 1996, *ApJ*, 470, 249
- Puccetti S., Fiore F., Risaliti G., Capalbi M., Elvis M., Nicastro F., 2007, *MNRAS*, 377, 607
- Radomski J. T., Piña R. K., Packham C., Telesco C. M., De Buizer J. M., Fisher R. S., Robinson A., 2003, *ApJ*, 587, 117
- Reynolds C. S., Fabian A. C., Makishima K., Fukazawa Y., Tamura T., 1994, *MNRAS*, 268, L55
- Ruiz M., Young S., Packham C., Alexander D. M., Hough J. H., 2003, *MNRAS*, 340, 733
- Rybicki G. B., Lightman A. P., 1979, *Radiative Processes in Astrophysics*. Wiley, New York
- Schurch N. J., Warwick R. S., 2002, *MNRAS*, 334, 811
- Schurch N. J., Warwick R. S., Griffiths R. E., Sembay S., 2003, *MNRAS*, 345, 423
- Schurch N. J., Warwick R. S., Griffiths R. E., Kahn S. M., 2004, *MNRAS*, 350, 1

- Shakura N. I., Sunyaev R. A., 1973, *A&A*, 24, 337
Shapovalova A. I. et al., 2008, *A&A*, 486, 99
Shimura T., Takahara F., 1995, *ApJ*, 445, 780
Ulvestad J. S., Wong D. S., Taylor G. B., Gallimore J. F., Mundell C. G., 2005, *AJ*, 130, 936
Wardziński G., Zdziarski A. A., Gierliński M., Grove J. E., Jahoda K., Johnson W. N., 2002, *MNRAS*, 337, 829
Wijers R. A. M. J., Pringle J. E., 1999, *MNRAS*, 308, 207
Xie F.-G., Niedźwiecki A., Zdziarski A. A., Yuan F., 2010, *MNRAS*, 403, 170
Yuan F., 2001, *MNRAS*, 324, 119
Yuan F., Zdziarski A. A., 2004, *MNRAS*, 354, 953
Zdziarski A. A., 1998, *MNRAS*, 296, L51
Zdziarski A. A., Johnson W. N., Magdziarz P., 1996a, *MNRAS*, 283, 193
Zdziarski A. A., Gierliński M., Gondek D., Magdziarz P., 1996b, *A&AS*, C120, 553
Zdziarski A. A., Poutanen J., Mikołajewska J., Gierliński M., Ebisawa K., Johnson W. N., 1998, *MNRAS*, 301, 435
Zdziarski A. A., Lubiński P., Smith D. A., 1999, *MNRAS*, 303, L11
Zdziarski A. A., Poutanen J., Johnson W. N., 2000, *ApJ*, 542, 703
Zdziarski A. A., Leighly K. M., Matsuoka M., Cappi M., Mihara T., 2002, *ApJ*, 573, 505 (Z02)
Zdziarski A. A., Lubiński P., Gilfanov M., Revnivtsev M., 2003, *MNRAS*, 342, 355

This paper has been typeset from a $\text{\TeX}/\text{\LaTeX}$ file prepared by the author.